coatings

MDPI

Article

A Comparative Study of Chloride Adsorption Ability and Corrosion Protection Effect in Epoxy Coatings of Various Layered Double Hydroxides

Yanhui Cao [1,2,*], Jingjing Wang [1,2], Kaifeng Chen [1,2], Xinyue Zhang [1,2], Bing Zhang [3], Shuo Fang [1,4], Yu Liang [1,2], Congshu Huang [1,2] and Xinyu Wang [3]

1 Luoyang Ship Material Research Institute, Xiamen 361101, China
2 Science and Technology on Marine Corrosion and Protection Laboratory, Xiamen 361101, China
3 China Ship Development and Design Center, Wuhan 430064, China
4 Liaoning Provincial Key Laboratory for Preparation and Application of Special Functional Materials, Shenyang University of Chemical Technology, Shenyang 110142, China
* Correspondence: yanhuicao@yeah.net; Tel.: +86-15506922136

Abstract: The positive influence of chloride adsorption on the enhanced protection effect was always emphasized in the published literature. The concrete contribution of chloride adsorption and physical barrier effect of LDH in coatings still remains unclear at present. This work was aimed at exploring the significance of the chloride adsorption role of LDH in the corrosion protection of epoxy coatings. The synthesized LDH samples were characterized by scanning electronic microscopy (SEM), X-ray diffraction (XRD) and Fourier transform infrared spectroscopy (FTIR) to show the influence of different parameters on its morphology, structure and composition, respectively. The corrosion-electrochemical behavior was investigated using electrochemical impedance spectroscopy (EIS) and salt spray test. It was found that although CaAl-LDH presented a lower chloride adsorption ability in comparison with other samples; it showed effective corrosion protection due to the higher physical barrier effect of CaAl-LDH with typically hexagonal and plate-like morphology due to good compatibility with the epoxy coatings. The results indicated that the corrosion protection effect of the incorporated LDH was more closely related to its physical barrier role rather than the role of the chloride adsorption, which was misunderstood in the previous publications. This work clarified the contribution comparison of the chloride adsorption and physical barrier of LDH in epoxy coating corrosion protection for the first time.

Keywords: layered double hydroxide (LDH); synthesizing parameters; chloride adsorption; barrier effect; corrosion protection

check for updates

Citation: Cao, Y.; Wang, J.; Chen, K.; Zhang, X.; Zhang, B.; Fang, S.; Liang, Y.; Huang, C.; Wang, X. A Comparative Study of Chloride Adsorption Ability and Corrosion Protection Effect in Epoxy Coatings of Various Layered Double Hydroxides. *Coatings* **2022**, *12*, 1631. https://doi.org/10.3390/coatings12111631

Academic Editor: Matjaž Finšgar

Received: 12 September 2022
Accepted: 20 October 2022
Published: 27 October 2022

1. Introduction

Corrosion occurs easily and widely in various environments. It has not only caused huge financial and resource loss but also led to frequent occurrence of safety accidents, which have posed severe challenges to the industrial production, human life and the sustainable development of our society. Therefore, various methods have been developed to prevent the occurrence and propagation of corrosion, including adoption of coatings, inhibitors and electrochemical protective methods, etc. [1–3]. Anti-corrosion protective coatings have been regarded as one of the most effective, convenient and cost-saving methods to prevent corrosion [4]. However, coatings usually have defects, holes and cavities, through which aggressive solution permeates into the coatings and reaches the underlying metal substrates; as a result, corrosion could be initiated in this way. The occurrence of corrosion shortened the service life of the coatings; therefore, efforts should be devoted to preparing high-quality coatings with fewer defects and holes to provide a better corrosion protection effect for the target metal substrates.

In the reported literature, layered double hydroxides (LDHs) have been added into various coatings to improve its corrosion protection ability due to its unique layered structure, anion-exchange characteristics and anion-containing property. For example, Liu et al. designed Ce-doped ZnAl layered double hydroxides (ZnAlCe-LDHs) and incorporated them into a hybrid sol-gel (SiOx/ZrOx) layer on aluminum AA2024. The sol–gel coating embedded with LDHs (Ce/(Al + Ce) = 0.1) exhibited high corrosion resistance probably due to the synergistic inhibition of ZnAlCe-LDHs and CeO_2 nanoparticles [5]. In addition, Mg-Al layered double hydroxides modified with benzotriazole (LDH-BTA) were synthesized using the co-precipitation method, which allows the reasonable barrier properties of the epoxy-based coating associated with a self-healing ability during immersion [6]. Epoxy coating incorporated with aminobenzoate intercalated Mg-Al layered double hydroxides (LDH) showed effective corrosion protection effect on steel reinforcement as reported by Mei et al. [7]. In addition, the CaAl-LDH loaded with 2-mercaptobenzothiazole (MBT) was synthesized and incorporated in epoxy resin as pigment with different content to improve the corrosion protection effect of coating on Q235 steel. The enhanced corrosion protection ability was attributed to the barrier effect, the chloride entrapment and the release of 2-mercaptobenzothiazole (MBT) [8]. Besides, the influence of incorporation of LDH on the mechanical properties of the coating also requires attention, since they are closely related to the practical application. Recently, Moustafa Mahmoud Yousry Zaghloul studied the fatigue and tensile behaviors of fiber-reinforced thermosetting composites embedded with nanoparticles [9]. The experimental results showed that the addition of 4% cellulose nanocrystals to polyester matrix led to the optimum tensile and fatigue properties. They also prepared the ecologically friendly flame-retardant melamine polyphosphate (MPP) and incorporated them into linear low-density polyethylene (LLDPE). It was concluded that the Young's modulus increased sharply, and the tensile break strength and the tensile yield strength increased monotonically with the increase in MPP content [10]. However, such an investigation has not been performed in the coating systems incorporated with LDH powders, which require further exploration.

In order to further improve the physical barrier effect of the coatings, other 2D materials such as graphene and its derivatives were combined with LDHs to further improve the corrosion protection ability of the coatings. For example, Xue et al. loaded vanadate anions (VO_x^-) and 2-mercaptobenzothiazole anions (MBT) into the grapheme oxides (GO)/LDHs nanocontainers and they were added into a sol-gel coating on AA2024-T3. The result indicated that the corrosion protection of the sol-gel coating was effectively improved [11]. The increased corrosion protection effect was caused by the enhancement of the barrier property from the good dispersion of the LDHs with the 2D structure and the good barrier of GO sheets, and the corrosion inhibition of vanadate anions. Nguyen et al. investigated the influence of molybdate intercalated hydrotalcitesHT-MoO_4/GO on corrosion resistance of waterborne epoxy coating applied on carbon steel. (HT-MoO_4)/GO at 1 wt% concentration improved corrosion resistance of waterborne epoxy coatings [12]. The presence of GO increased the effects of HT-MoO_4 on protection properties of waterborne epoxy coatings. Similarly, basalt scales (Bt) were modified with polydopamine (PDA) to introduce active sites by Zhang et al. [13], followed by in-situ growth of molybdate-loaded layered double hydroxide (LM) on the surface of PDA-modified basalt. The excellent corrosion resistance of the coating can be attributed to the synergistic effect of barrier property, chloride ion trapping effect and corrosion inhibition of the obtained filler.

It can be concluded that the dispersion state, chloride adsorption ability and the inhibitor releasing behavior can be regarded as three significant factors contributing to the overall corrosion protection ability. It should be noted that the inhibitor release was closely related to the chloride adsorption ability based on the anion-exchange reaction, and higher chloride adsorption ability usually indicated a higher inhibitor anion capacity.In our previously published work, the MgAl-LDH and ZnAl-LDH powder samples intercalated with various inhibitors were synthesized and characterized, and they were then added in concrete and the corresponding corrosion protection mechanism in reinforced concrete was

investigated [14–16]. In addition, the ZnAl-LDH films on Al substrate were also prepared and multifunctional modification towards it was carried out, and the corrosion protection mechanism was also studied deeply [17–19]. In the published literature, the role of chloride adsorption was always highlighted [13,20,21]. However, the concrete contribution of the role of chloride adsorption and physical barrier still remains unclear. This work was mainly aimed at exploring the contribution of chloride adsorption role of LDH powder on the corrosion protection ability when no inhibitors are intercalated in epoxy coating for the first time, which was totally different from what has already been done in the published work. The relationship between the chloride adsorption ability and the final obtained corrosion protection ability was firstly evaluated in a practical system, which shed light on the comparison of significance of chloride adsorption ability and physical barrier effect in the final corrosion protection.

2. Experimental

2.1. Materials and Agents

$Mg(NO_3)_2 \cdot 6H_2O$, $Al(NO_3)_3 \cdot 9H_2O$, $Ca(NO_3)_2 \cdot 4H_2O$, $Zn(NO_3)_2 \cdot 6H_2O$, $NaNO_3$, NaOH, HCl and NaCl were purchased from Sinopharm Chemical Reagent Co. Ltd. (Beijing, China). All the agents were analytical grade, and all the solutions were prepared with deionized water. 6101 epoxy resin and the 2519 hardener were provided by Shanghai Dekun Industrial Co., Ltd. (Shanghai, China); N-butyl alcohol was ordered from Baling Petroleum & Chemical Co. Ltd. (Yueyang, China). Q235 plate with the size of 75 mm × 150 mm × 2 mm was provided by Xiamen Qianfeng Mechanical Co. Ltd. (Xiamen, China). Dispersants (BYK-110), leveling agents (BYK-320) and antifoaming agents (BYK-530) were ordered from Bike Chemial Co. Ltd. (Tongling, China). The main physical and chemical properties of the raw materials used in this study were listed in Tables 1–3.

Table 1. The main physical and chemical properties of assistant agent.

Items	BYK110	BYK320	BYK 580
Solvent	**Propylene Glycol Methyl Ether Acetate/Alkyl Benzene (1/1)**	**Petroleum Solvent /Propylene Glycol Methyl Ether Acetate (9/1)**	**Hydrocarbon Mixture (Paraffin Series, Naphthenic Series)**
Density (20 °C g/mL)	1.03	0.86	0.81
Non volatile matter %	52	52	5
Flash point (°C)	42	38	>95

Table 2. The main physical and chemical properties of 6101 epoxy resin.

Items	6101 Epoxy Resin
Epoxy equivalent (g/eq)	210–240
softening point (°C)	12–20
viscosity (25 °C mPa·s 80% Xylene solution)	200–400
Saponifiable chlorine (%)	<=0.3
Inorganic chlorine (ppm)	<=180

Table 3. The main physical and chemical properties of 2519 hardener.

Items	2519 Hardener
Viscosity (25 °C mPa·s)	185
Density (25 °C g/mL)	1.01
Flash point (°C)	>100
Amine value (mg KOH/g)	315

2.2. LDHs Preparation

2.2.1. Changing the Divalent Cations

200 mL mixed solution containing 0.5 mol/L $Ca(NO_3)_2$ and 0.25 mol/L $Al(NO_3)_3$ was added drop wisely into 100 mL mixed solution of 2 mol/L $NaNO_3$ and 3 mol/L NaOH with rigorous magnetic stirring at 65 °C. After the above co-precipitation process, the obtained slurry was transferred to the stainless hydrothermal reactor. The hydrothermal reaction was performed at 120 °C for 24 h. Then the product was washed by deionized water and centrifuged, and the final obtained product was labeled as Ca2Al1-LDH. For the synthesis of Mg2Al1-LDH, $Mg(NO_3)_2{\cdot}6H_2O$ was used instead of $Ca(NO_3)_2{\cdot}4H_2O$. For the synthesis of Zn2Al1-LDH, $Zn(NO_3)_2{\cdot}6H_2O$ was used instead of $Ca(NO_3)_2{\cdot}4H_2O$. This synthesis procedure was referred to the literature [22,23].

2.2.2. Changing the Divalent to Trivalent Cation Ratios

The 200 mL mixed solution containing 0.5 mol/L $Zn(NO_3)_2$ and 0.17 mol/L $Al(NO_3)_3$ was added drop wisely into 100 mL mixed solution of 2 mol/L $NaNO_3$ and 3 mol/L NaOH with rigorous magnetic stirring at 65 °C. After the above co-precipitation process, the obtained slurry was transferred to the stainless hydrothermal reactor. The hydrothermal reaction was performed at 120 °C for 24 h. Then the product was washed by deionized water and centrifuged, and the final obtained product was labeled as Zn3Al1-LDH. For the synthesis of Zn4Al1-LDH, 0.125 mol/L $Al(NO_3)_3$ was used instead of 0.17 mol/L $Al(NO_3)_3$ in the above process. This synthesis procedure was referred to in the literature [22,23].

2.2.3. Changing the Hydrothermal Time

As described in Section 2.2.1, the hydrothermal time of ZnAl-LDH was set as 6 h and 15 h instead of 24 h, and the corresponding sample was designated as Zn2Al1-LDH-6h, Zn2Al1-LDH-15h and Zn2Al1-LDH-24h, respectively.

2.3. LDHs Sample Characterization

The morphology and elemental composition were characterized by scanning electronic microscopy (SEM, ZEISS ULTRA55, Carl Zeiss AG Co. Ltd., Dresden, Germany) coupled with energy dispersive spectrometer (EDS, Carl Zeiss AG Co. Ltd., Dresden, Germany). The crystalline structure was studied by X-ray diffraction (XRD, X'Pert PRO, Malvern PANalytical Co. Ltd., Almelo, The Netherlands) with the applied voltage was 40 kV and the current was 40 mA. The samples were scanned from 5 to 80° with a scanning rate of 10°/min. The chemical composition was presented by Fourier transform infrared spectroscopy (FTIR, Nicolet IN10, Thermo Fisher Scientific Co. Ltd., Waltham, MA, USA). The scanning ranged from 400–4000 cm^{-1} with a resolution of 4 cm^{-1} and 64 scans.

2.4. LDHs Chloride Adsorption Ability Evaluation

LDHs was added into 0.02 mol/L NaCl with a concentration of 10 g/L, which was then subjected to rigorous magnetic stirring for certain time. Ag/AgCl probe was used to detect the chloride changes, which was prepared by an anodization method as described in our previously published work [22].

2.5. Coating Preparation

2 g LDHs (2 wt.% of EP) sample was added into 50 mL N-butyl alcohol, and it was then subjected to rigorous stirring for 30 min and ultrasonication for 30 min subsequently to obtain well-dispersed solution. After that, this solution was mixed with 100 g 6101 epoxy resin, and 1 g dispersants (BYK-110), 1 g leveling agents (BYK-320) and 1 g antifoaming agents (BYK-580) were also incorporated into the above mixture. This mixture was stirred for 1 h at 1000 r/min, and it was then placed at room temperature overnight to remove the produced bubbles during high-speed stirring, which was labeled as component A.

6101 epoxy resin and the 2519 hardener (Component B) was mixed at a weight ratio of 100:42, thus the ratio between the Component A described above and the hardener was

155:42. A wooden rod was used to mix Component A and B to obtain a uniform mixture. A small brush was adopted to apply the coating on the Q235 plate evenly and the thickness of the wet film was measured by a wet film thickness gauge. The Q235 plate with a wet film thickness of around 75 μm was chosen and was cured in ambient atmosphere for 2 d. Then it was further applied with the coating using a brush once again. Similarly, the sample with a wet film thickness of around 75 μm was chosen. It can be seen that the total thickness of the wet coating was controlled around 150 μm. As the solid content of the coating was calculated to be 74.6%, the thickness of the final obtained dry coating was kept between 110 ± 10 μm, appropriately. This coating preparation procedure was referred to in the published literature [24].

2.6. Coating Morphology and Roughness Characterization

The top-view and side-view morphology of the epoxy coating with and without addition of LDHs was characterized by SEM (ZEISS ULTRA55, Carl Zeiss AG Co. Ltd., Drresden, Germany). For SEM characterization, The SEM images were captured with the Inlens mode, where signals from secondary electrons were collected. The accelerating voltage was 3 kV, and the working depth varies in the range of 3 to 5 mm due to the different height of various samples.

The coating 3D morphology was characterized by laser microscopy (OLS5000, Olympus Co. Ltd., Tokyo, Japan). The roughness (arithmetical mean height) was characterized through the zone method based on 3D morphology and presented through the software automatically. The test was repeated three times in three different areas.

2.7. Corrosion Protection Property Investigation

2.7.1. Electrochemical Impedance Spectroscopy (EIS) Test

A PVC pipe with an internal diameter of 5.7 cm was fixed on the surface of the coated steel panel with silastic. 3.5 wt.% was added to simulate the sea water. The EIS tests were carried out on an Electrochemical Impedance Analyzer (Wuhan Kesite Instrument Co. Ltd., Wuhan, China). Ag/AgCl (R0305) was used as the reference electrode, the steel plate was used as the working electrode, and a platinum (2 cm × 2 cm) was used as the counter electrode, respectively. The EIS test was performed according to ISO 16773–2016 [25]. The scanning frequency range was from 10^5–10^{-2} Hz and the adopted disturbing amplitude of 10 mV. The EIS test was performed after immersion in 3.5 wt.% NaCl solution for 1 d, 3 d, 7 d, 14 d and 21 d.

2.7.2. Salt Spray Test

The salt spray test was carried out in a salt spray chamber with CCT-1100 model according to GB/T1771-2007 [26]. The temperature in the salt spray chamber was (35 ± 2) °C, and the collected NaCl concentration was (50 ± 10) g/L. The samples were exposed in the salt spray chamber until 21 d. Digital pictures were captured by a camera at a certain time to record the changes of sample surface.

3. Results and Discussion

3.1. Characterization

3.1.1. SEM and EDS Results

The SEM and corresponding EDS results of different samples with different divalent cations are shown in Figure 1. It is revealed that Ca2Al1-LDH presents obvious hexagonal plate-like morphology with size ranging from 2 μm to 20 μm approximately, and this result was analogous to the literature [8]. C, O, Al and Ca appeared in the EDS spectrum, and the atomic ratio of Ca/Al was 1.67, which was close to the theoretical value of 2. As for Zn2Al1-LDH in Figure 1b, the sample demonstrated plate-like morphology with random shape instead of hexagonal shape, which differed from that of Ca2Al1-LDH greatly. The aggregation phenomenon can be observed in the case of Zn2Al1-LDH. The EDS results showed the element of C, O, Zn and Al with a Zn/Al atomic ratio of 1.60. According

to Figure 1c, the Mg2Al1-LDH exhibited uniform and hexagonal shape with the size of 150 nm appropriately. Its EDS results in Figure 1c demonstrated a Mg/Al ratio of 1.87, which was in good accordance with the theoretical value.

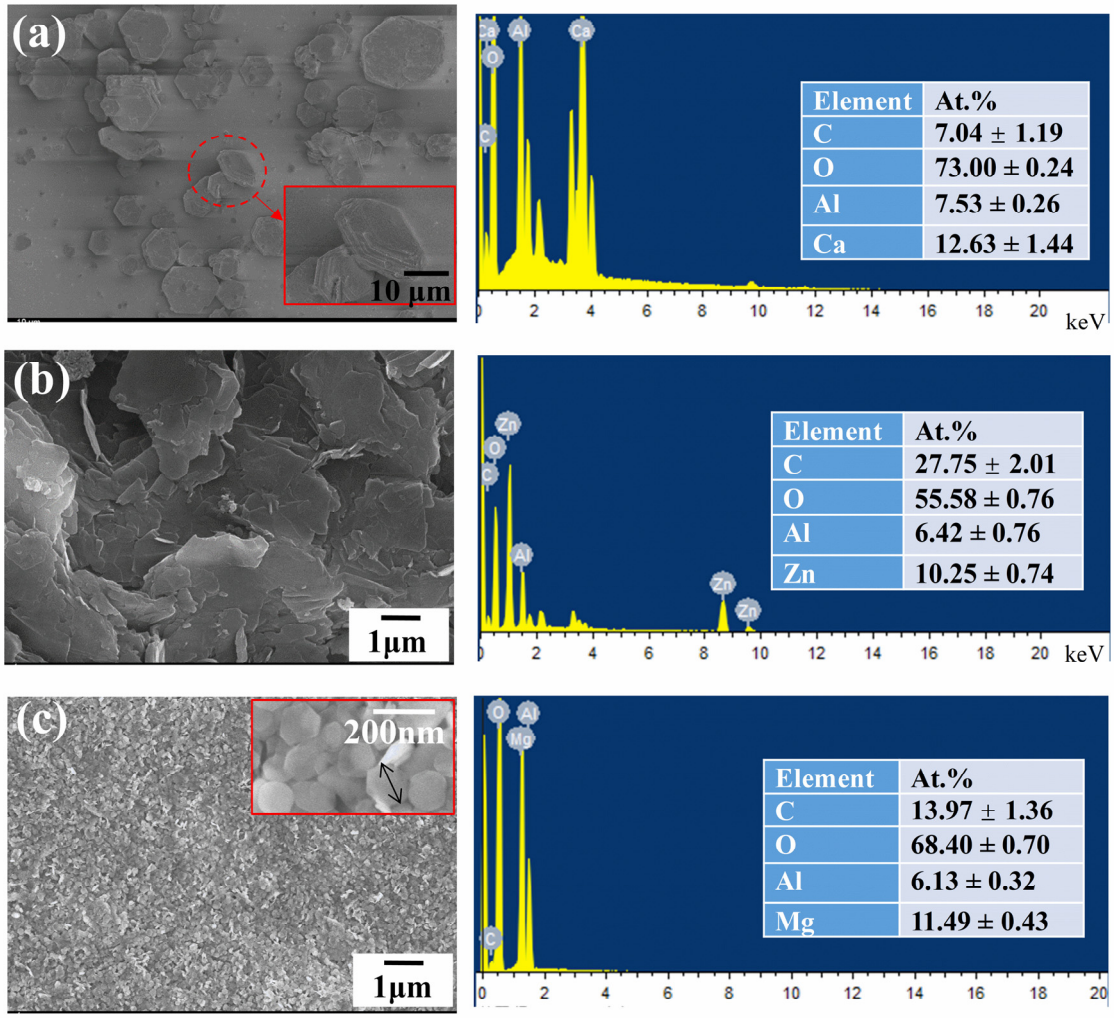

Figure 1. The SEM and corresponding EDS results of (**a**) Ca2Al1-LDH, (**b**) Zn2Al1-LDH, (**c**) Mg2Al1-LDH.

The influence of varied divalent to trivalent ratios on the morphology and elemental composition is shown in Figure 2. It can be seen that Zn2Al1-LDH presented single plate-like morphology, while in the case of Zn3Al1-LDH, two kinds of particles with different morphology appeared. One is the phate-like morphology, which is similar to that in Figure 2a. The elemental composition in the EDS result is also in good agreement with that in Figure 2a. The other is rod-like morphology, which can be attributed to ZnO based on the obviously increased content of Zn in the EDS result. According to Figure 2c, the synthesized sample can be mainly attributed to ZnO when the divalent to trivalent ratio further increased to 4, indicating that ZnAl-LDH cannot be formed in this case, successfully.

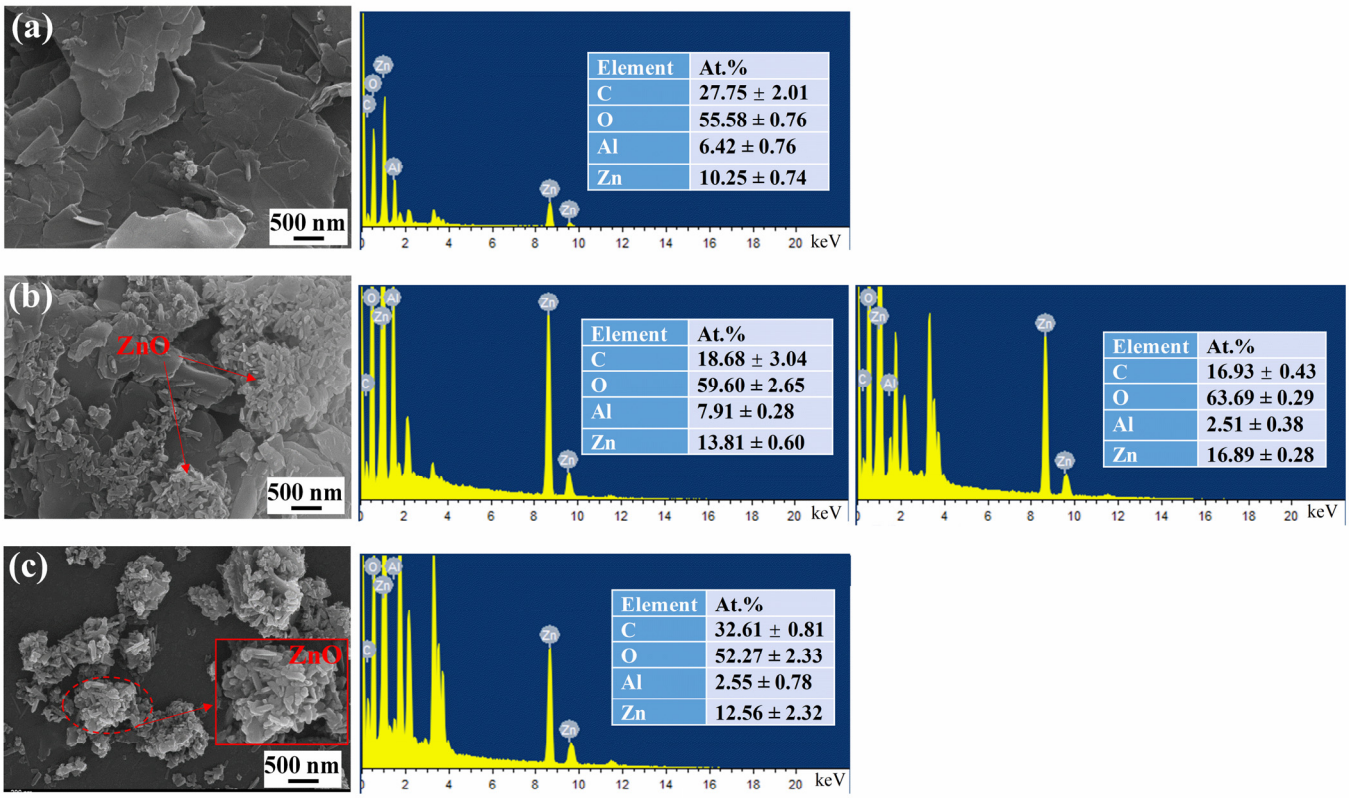

Figure 2. The SEM and corresponding EDS results of (**a**) Zn2Al1-LDH, (**b**) Zn3Al1-LDH, (**c**) Zn4Al1-LDH.

In the published literature, many researchers carried out hydrothermal treatment of 24 h in the synthesis of LDH powders [8,23,27]. A shorter hydrothermal time to prepare LDH powders was rarely adopted in the reported work. In order to investigate the influence of hydrothermal time on the structure, morphology, composition and chloride adsorption ability systematically, the hydrothermal treatment time of 6, 15 and 24 h were chosen in this work. The influence of hydrothermal time on the morphology and composition of the LDHs samples is shown in Figure 3. It can be seen that the platelet-like morphology was presented when the hydrothermal time was 6 h, 15 h and 24 h. The particle size increased slightly, and the Zn/Al ratio almost kept constant when the hydrothermal time was prolonged. The C content increased obviously from 12.56% to 27.75% when the hydrothermal time was increased from 6 h to 24 h due to more contamination from CO_2 upon increased reaction time.

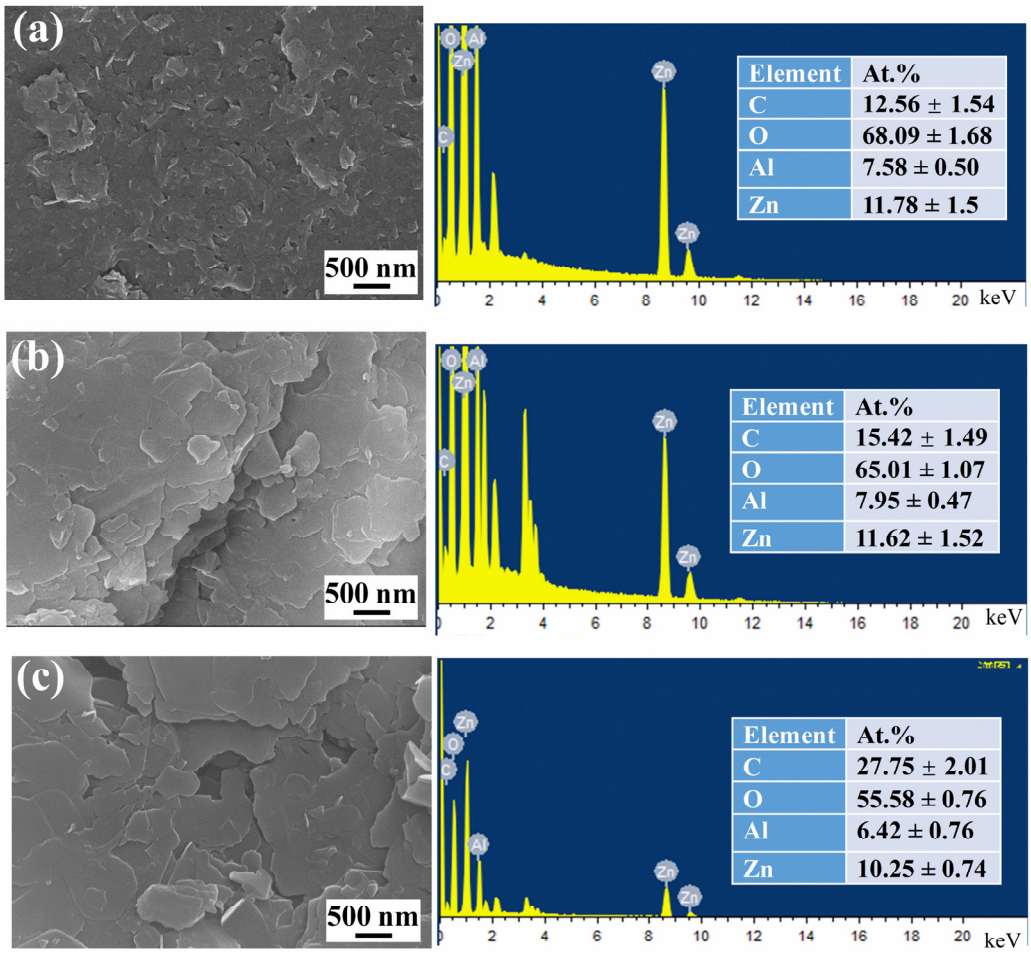

Figure 3. The SEM and corresponding EDS results of (**a**) Zn2Al1-LDH-6h, (**b**) Zn2Al1-LDH-15h, (**c**) Zn2Al1-LDH-24h.

3.1.2. XRD Results

The XRD results of LDHs samples with different divalent cations are listed in Figure 4. According to Figure 4a, it can be seen that all the three samples presented typical crystalline (003) and (006) planes of LDHs samples, indicating successful preparation of CaAl-LDH, ZnAl-LDH and MgAl-LDH [28]. The position of (003) planes of the three samples appeared at around 10°, verifying the main intercalation of nitrates in the LDH galleries [29,30]. As the peaks in the range of 25–80° cannot be seen clearly in Figure 4a, the spectrum from 25 to 80° as magnified, which are shown in Figure 4b–d. It is clear from Figure 4b that the peaks of $CaCO_3$ appeared in the spectrum of Ca2Al1-LDH. In the XRD spectrum of Zn2Al1-LDHin Figure 4c, the peaks of ZnO appeared, indicating the formation of some ZnO during the synthesis of Zn2Al1-LDH. In Figure 4d, a peak corresponding to MgO occurred in the spectrum of Mg2Al1-LDH. The above results suggested that corresponding metal oxides of divalent cations can be formed inevitably under the current synthesizing conditions, and the synthesizing parameters can be further adjusted to prepare LDH samples with higher purity.

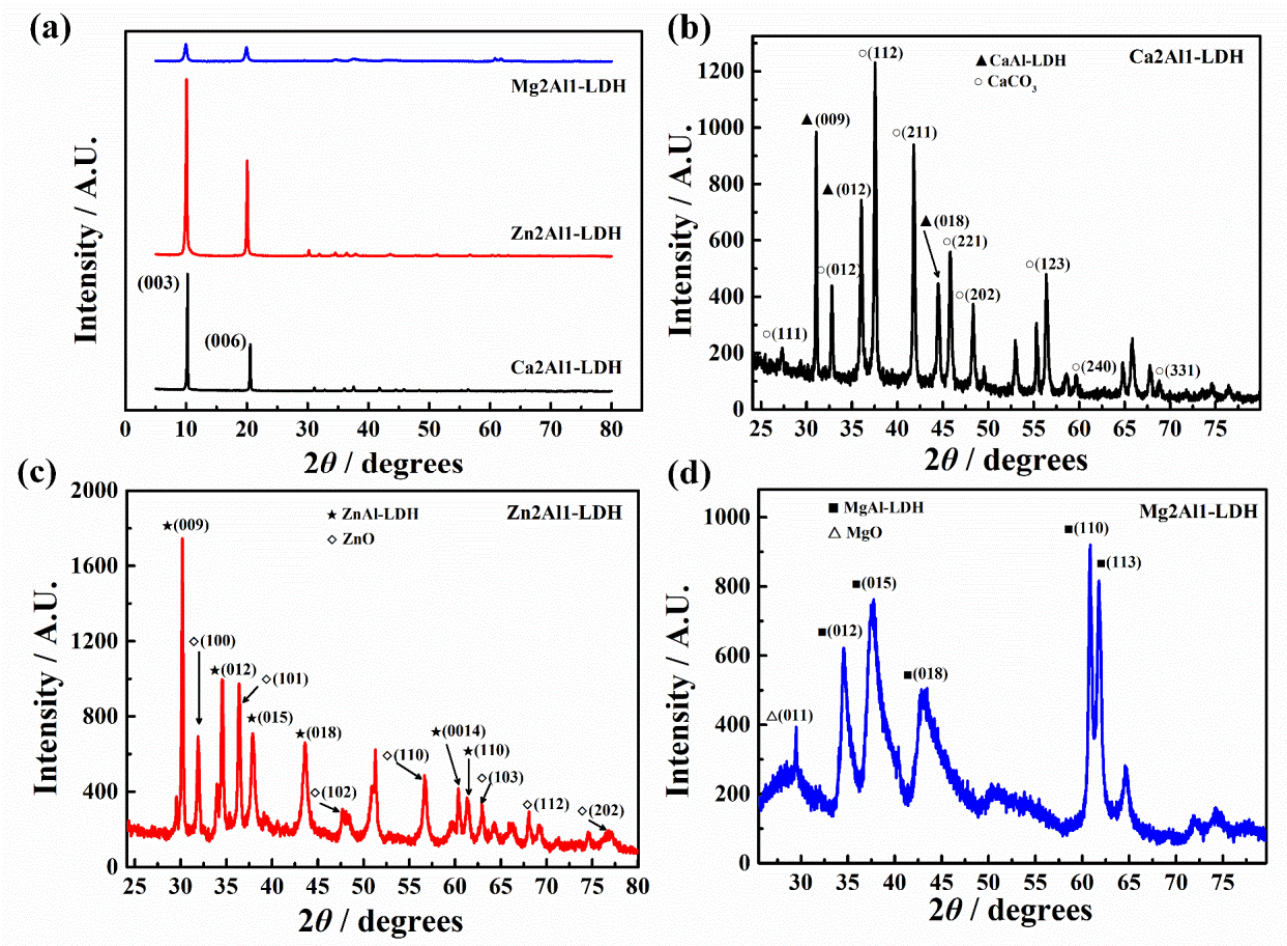

Figure 4. The XRD results of (**a**) Ca2Al1-LDH, Zn2Al1-LDH and Mg2Al1-LDH from 5 to 80°; (**b**) Ca2Al1-LDH from 24 to 80°; (**c**) Zn2Al1-LDH from 24 to 80°; (**d**) Mg2Al1-LDH from 24 to 80°.

The XRD spectrum of ZnAl-LDH samples with different divalent cation to trivalent cation ratios are shown in Figure 5. It can be seen that Zn2Al1-LDH presented peaks corresponding to (003) and (006) planes with higher intensities. In addition, small peaks of ZnO can also be observed. Zn3Al1-LDH also showed peaks related to (003) and (006) planes with lower intensities in comparison with that of Zn2Al1-LDH, and peaks of ZnO also appeared in its spectrum. For Zn4Al1-LDH, the peaks attributed to ZnAl-LDH cannot be observed while peaks of ZnO were obvious, suggesting the main formation of ZnO instead of ZnAl-LDH when the Zn/Al ratio increased to 4. The appearance of ZnO in the case of Zn3Al1-LDH and the full formation of ZnO in the case of Zn4Al1-LDH were in good agreement with the EDS result in Figure 2. According to the above result and analysis, it can be concluded that the Zn/Al ratio of 2 is more appropriate for successful preparation of LDH with low impurities.

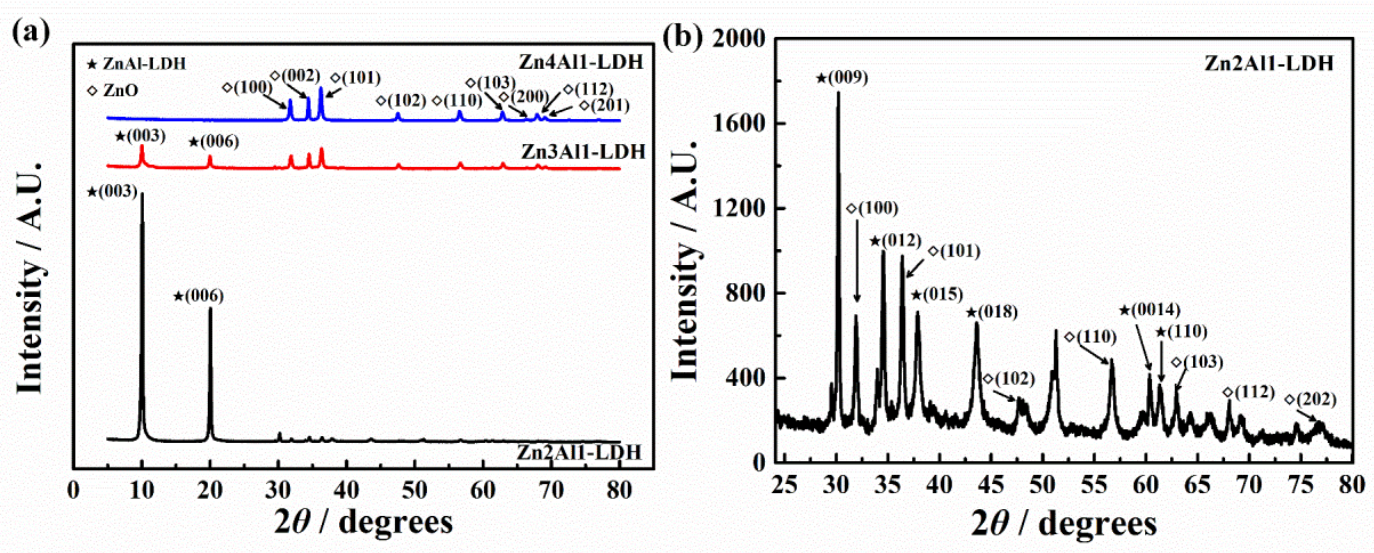

Figure 5. The XRD spectrum of (**a**) Zn2Al1-LDH, Zn3Al1-LDH and Zn4Al1-LDH; (**b**) Zn2Al1-LDH from 24 to 80°.

The ZnAl-LDH samples synthesized at different hydrothermal time are shown in Figure 6. It can be seen that the intensity of the peaks corresponding to (003) and (006) planes increased remarkably upon the prolonged hydrothermal time. The spectrum in the range of 25–80° were magnified to obtain more details as shown in Figure 6b–d. It is clear from Figure 6b,c that only peaks related to ZnAl-LDH can be observed in the sample of Zn2Al1-LDH-6h and Zn2Al1-LDH-15h, while some small peaks of ZnO appeared in the case of Zn2Al1-LDH-24h. The above result demonstrated that undesirable ZnO can be formed when the hydrothermal time was prolonged to 24 h in spite of higher intensity, this phenomenon was in good agreement with the finding of the literature that longer reaction time promoted the content of the by-products [31]. The result suggested that hydrothermal time should be controlled to a reasonable limit.

According to the literature, a sharper peak with higher intensity generally indicates improved crystallinity [32–34]. Based on the results in Figures 4–6, it can be summarized that the crystallinity of the synthesized LDH samples was influenced by different divalent cations, divalent to trivalent cation ratios, and hydrothermal time. The above results in Figures 4–6 indicated that Zn2Al1-LDH-24h presented the significantly increased crystallinity in comparison with LDH samples synthesized with other parameters.

The XRD spectrum was also used to investigate the anion-exchange process between the intercalated nitrates in LDHs gallery and the chloride anions in the environment. It should be noted that only the spectrum in the range of 5–25° was shown here because the changes of (003) plane are enough to provide rich information for the anion-exchange reaction. According to Figure 7a, it can be seen that the peak of (003) plane of the sample Ca2Al1-LDH was split into two peaks, where the prominent peak can be attributed to carbonates and the small one can be assigned to the intercalated chlorides due to the anion exchange reaction between nitrates and chlorides [35–37]. The intercalation of lots of carbonates into the gallery may be due to the strong interaction between the carbonates and the Ca^{2+} cations in the hydroxide layer. For Zn2Al1-LDH, the peak related to (003) plane was also split into two peaks, where one corresponded to the remaining nitrates in the LDH gallery and the other was due to the intercalated chloride anions. This result suggested that the anion-exchange reaction was not complete in this case. For Mg2Al1-LDH, only the peak corresponding to chlorides can be observed, indicating a complete anion-exchange reaction.

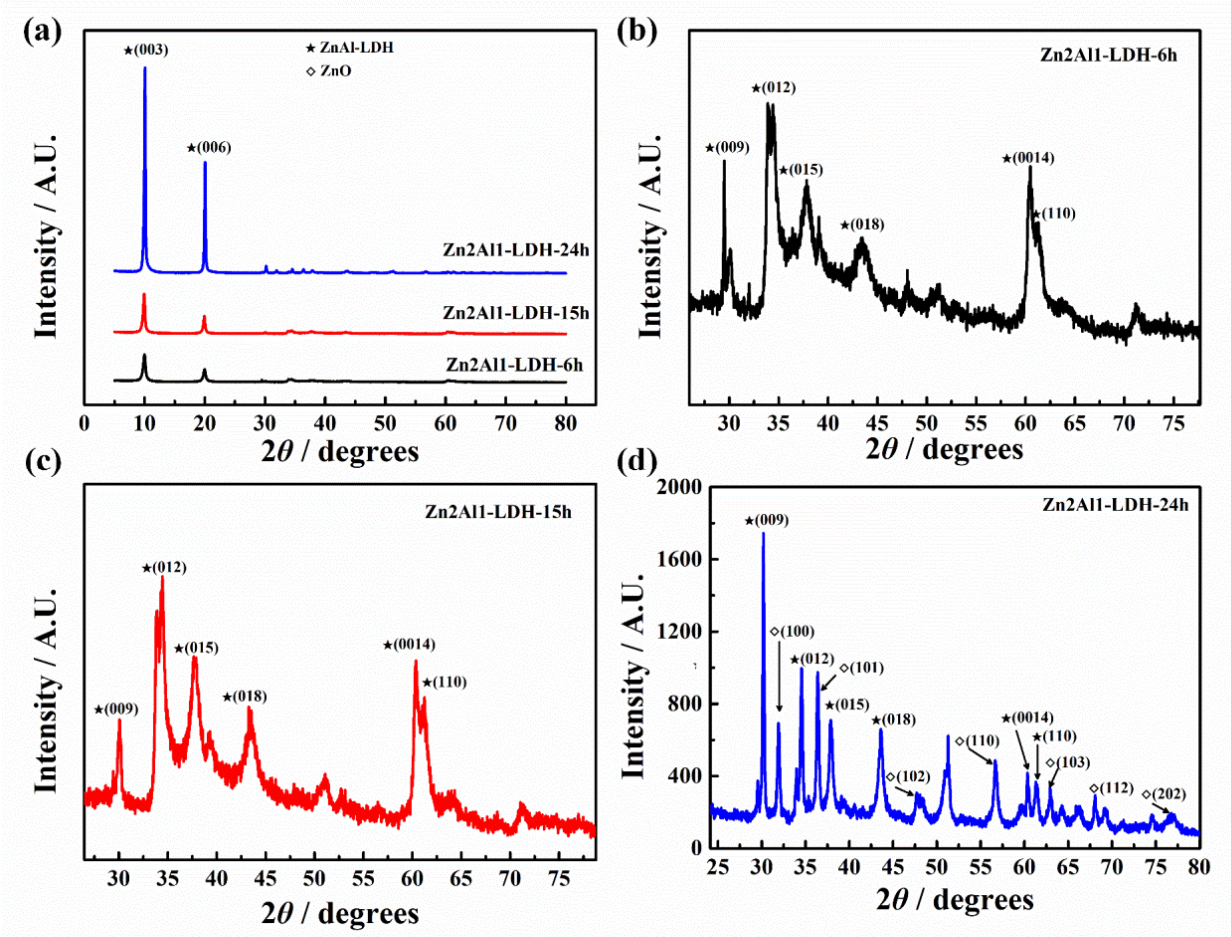

Figure 6. The XRD spectrum of (**a**) ZnAl-LDH synthesized at different hydrothermal time; (**b**) Zn2Al1-LDH-6h from 24 to 80°; (**c**) Zn2Al1-LDH-15h from 24 to 80°; (**d**) Zn2Al1-LDH-24h from 24 to 80°.

According to Figure 7b, almost no peaks can be found in the spectrum of Zn4Al1-LDH since only ZnO was formed when the Zn/Al ratio was 4, as interpreted above. The peak of (003) plane of Zn3Al1-LDH can be attributed to the intercalated chlorides, suggesting that all the nitrates in the LDH gallery have been replaced by chlorides. As stated above, Zn2Al1-LDH demonstrated a split peak of (003) plane due to the incomplete anion-exchange reaction, suggesting a higher anion capacity in the LDH gallery.

In Figure 7c, the XRD spectrum of ZnAl-LDH synthesized at different time are listed. It can be seen that the peaks of (003) plane of all these three samples were split into two peaks, corresponding to the remaining nitrates and the intercalated chlorides. This finding suggested that the anion-exchange between the nitrates in the gallery and the chlorides in the external environment was not complete in a period of 40 h, demonstrating a relatively higher anion capacity of the LDH gallery in comparison with the samples in Figure 7a,b. In other words, the nitrates in the LDH gallery cannot be replaced by chlorides completely in 40 h. In addition, the intensity of the peak corresponding to nitrates was higher than that of chlorides in the case of Zn2Al1-LDH-15h, while it was opposite in the case of Zn2Al1-LDH-24h. This phenomenon demonstrated that during an immersion period of 40 h the amount of the remaining nitrates in the gallery of Zn2Al1-LDH-15h was higher than that in Zn2Al1-LDH-24h, suggesting a relatively higher anion capacity and thus chloride adsorption ability of Zn2Al1-LDH-15h.

Therefore, the sample Zn2Al1-LDH-15h was further immersed in 0.02 mol/L NaCl solution for another 40 h, the obtained XRD result is shown in Figure 8. It can be seen that the (003) plane of Zn2Al-LDH-15h occurred at the position of 11.5°, corresponding to

the intercalated chlorides. No peaks related to nitrates can be observed, indicating that anion-exchange reaction between the nitrates and chlorides was complete after immersion for 80 h.

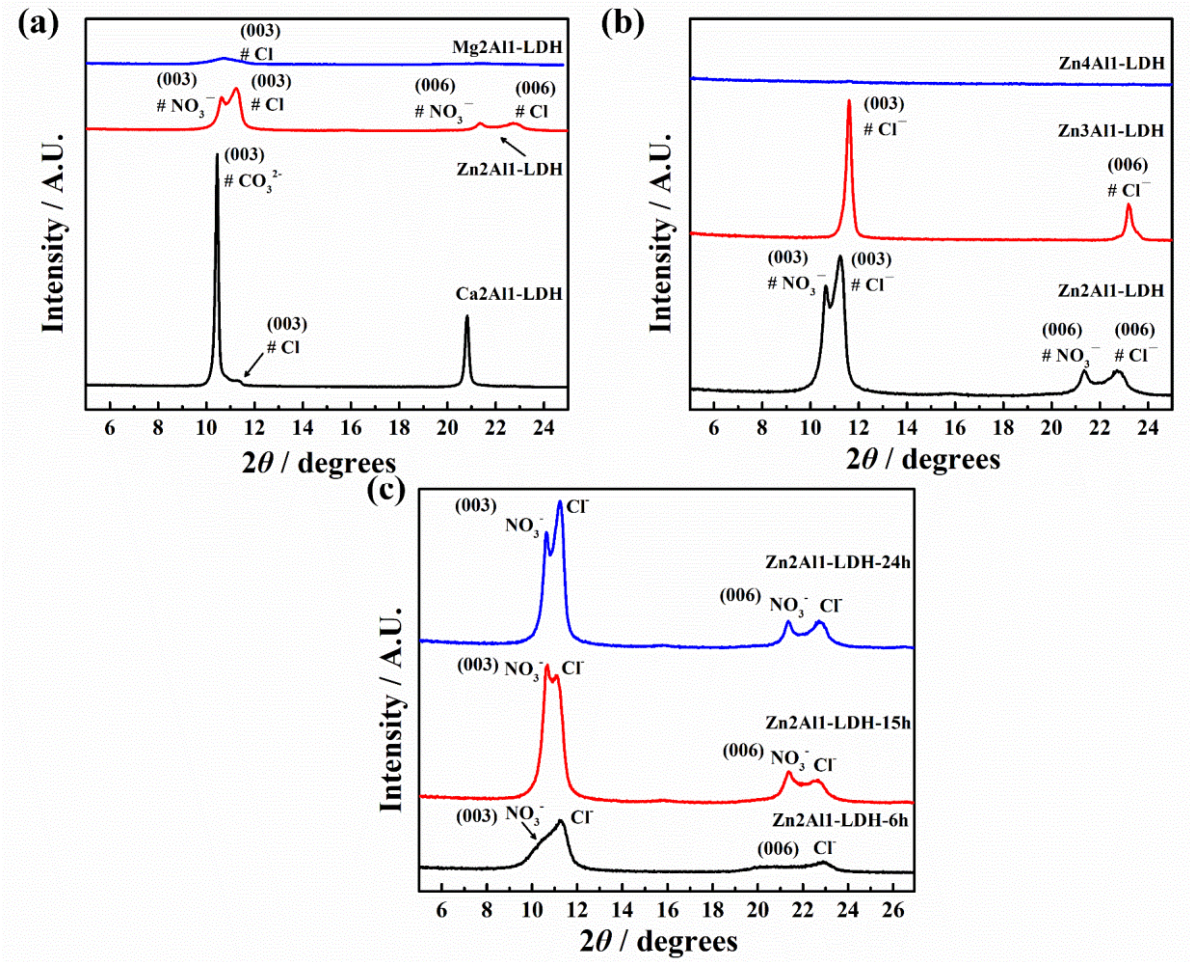

Figure 7. The XRD spectrum of different samples after immersion in 0.02 mol/L NaCl solution for 40 h (**a**) Ca2Al1-LDH, Zn2Al1-LDH and Mg2Al1-LDH; (**b**) Zn2Al1-LDH, Zn3Al1-LDH and Zn4Al1-LDH; (**c**) Zn2Al1-LDH-6h, Zn2Al1-LDH-15h and Zn2Al1-LDH-24h.

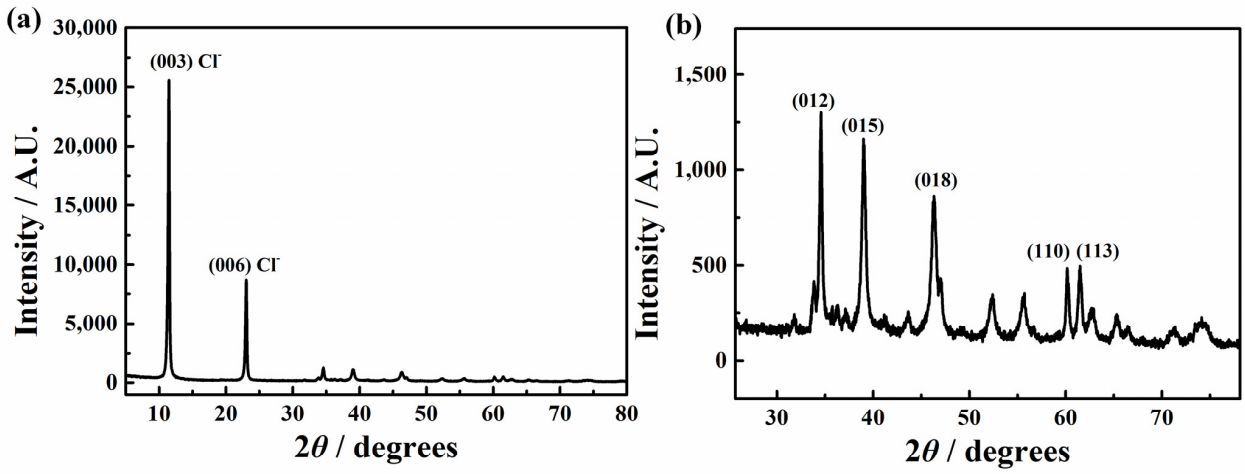

Figure 8. The XRD spectra of Zn2Al-LDH-15h after immersion in 0.02 mol/L NaCl solution for 80 h (**a**) from 5 to 80°; (**b**) from 25 to 78°.

3.1.3. FTIR Results

The FTIR measurements of various LDHs samples before and after immersion in NaCl solution were carried out to further provide more detailed information about composition, the results are shown in Figure 9. The peaks below 1000 cm^{-1} can be attributed to the M-O and M-O-H in the hydroxide layers [38]. Only the spectra of Zn4Al1-LDH showed no characteristic peaks of anions or chemical bond due to the unsuccessful formation of LDHs; the spectrum of other samples presented similar shape. The broad peaks from 3000–3700 cm^{-1} were due to the stretching vibration of O–H in interlayer water molecules and the peaks around 1630 cm^{-1} were due to bending vibration of H_2O [31]. According to Figure 9a–c, the peaks in the range of 1300–1500 cm^{-1} exhibited asymmetric shape with a shoulder at a relatively higher wavenumber, which can be attributed to the co-intercalation of nitrates and carbonates [32,39,40]. The carbonates can be intercalated into the LDH gallery inevitably due to its strong affinity with the hydroxide layers and CO_2 contamination is difficult to be avoided in the industrial production practically. During the immersion in NaCl solution for 40 h, the anion-exchange reaction occurred, therefore, some or all the nitrates in the gallery were replaced by the aggressive chlorides while the carbonates can be hardly substituted by other anions due to the strong affinity with the hydroxide layers. According to the FTIR spectra of Zn3Al1-LDH in Figure 9e, only a symmetric peak at 1352 cm^{-1} appeared, indicating that nitrates almost disappeared completely in the LDHs gallery. This result was in good accordance with the XRD result of Zn3Al1-LDH in Figure 7b. It can be concluded that in the case of Zn3Al1-LDH, the anion-exchange reaction was complete and almost all the nitrates in the LDH gallery were replaced by the chlorides due to a low anion capacity. As for other samples in Figure 9d,e, it can be seen that the peak at 1360 cm^{-1} was split into two peaks obviously, where one appeared at around 1350 cm^{-1}, and the other peak appeared at around 1420 cm^{-1}, which corresponded to the carbonates and the remaining nitrates in the LDHs gallery, respectively. These FTIR results were in good agreement with the XRD result in Figure 7 perfectly.

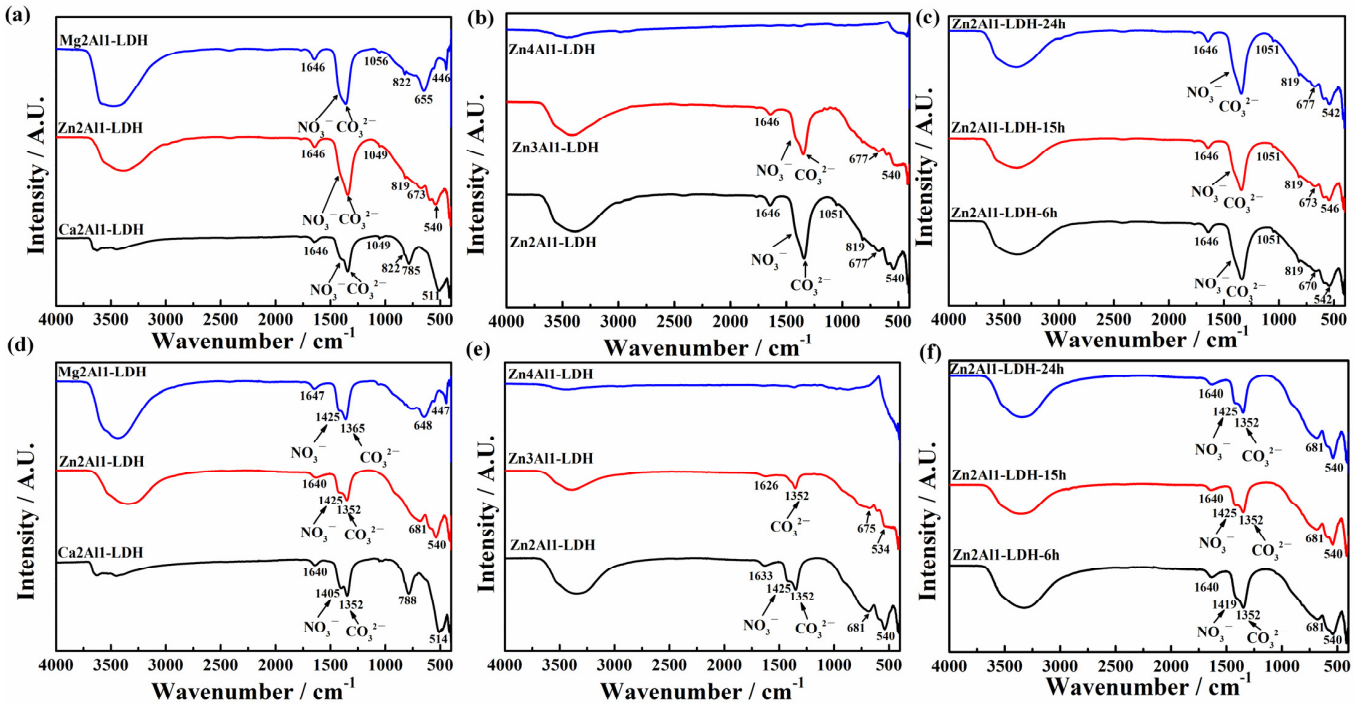

Figure 9. The FTIR results of different LDHs samples: (**a**–**c**) as-prepared; (**d**–**f**) after immersion in 0.02 mol/NaCl for 40 h.

3.2. Chloride Adsorption Ability

The equilibrium chloride concentration C_e decreased to different extent with the addition of different LDHs samples. It can be seen that ZnAl-LDH showed a highest reduction of 51% in comparison with the value of 15% and 39% of CaAl-LDH and MgAl-LDH, respectively, indicating superior chloride adsorption ability of ZnAl-LDH. When the Zn/Al ratio was changed from 2 to 4, the reduction percentage of chloride decreased obviously. This can be explained by the fact of formation of a larger amount of ZnO and decreased crystallinity of obtained ZnAl-LDH upon the increase of Zn/Al ratio as supported by the SEM, EDS and XRD result. As for the influence of hydrothermal time on the LDHs samples' chloride adsorption ability, the ZnAl-LDH sample synthesized at 15 h exhibited the largest reduction of chloride concentration with a percentage of 65.4% in comparison with that of the sample synthesized at 6 h (53.4%) and 24 h (51.2%). According to the XRD result in Figure 6a, although ZnAl-LDH synthesized at 24 h showed increased crystallinity, the slight decrease in the chloride reduction percentage may be probably due to the partial formation of ZnO.

According to our previous publication, the amount of chloride adsorption at the equilibrium Q_e (mg g^{-1}) was calculated according to Equation (1) [22,41,42]:

$$Q_e = \frac{1000(C_0 - C_e)VM}{m} \quad (1)$$

where C_0 and C_e is the initial and equilibrium chloride concentration (mol/L), respectively. V is the solution volume (L), and M is the molar mass of Cl element with a value of 35.5 mol/g, m is the mass of LDH (g).

According to Figure 10d–f, Q_e of different LDHs samples presented a completely opposed changing trend in comparison with that of C_e. Among all the samples, Zn2Al1-LDH synthesized at 15 h presented a high Q_e of 46 mg g^{-1}.

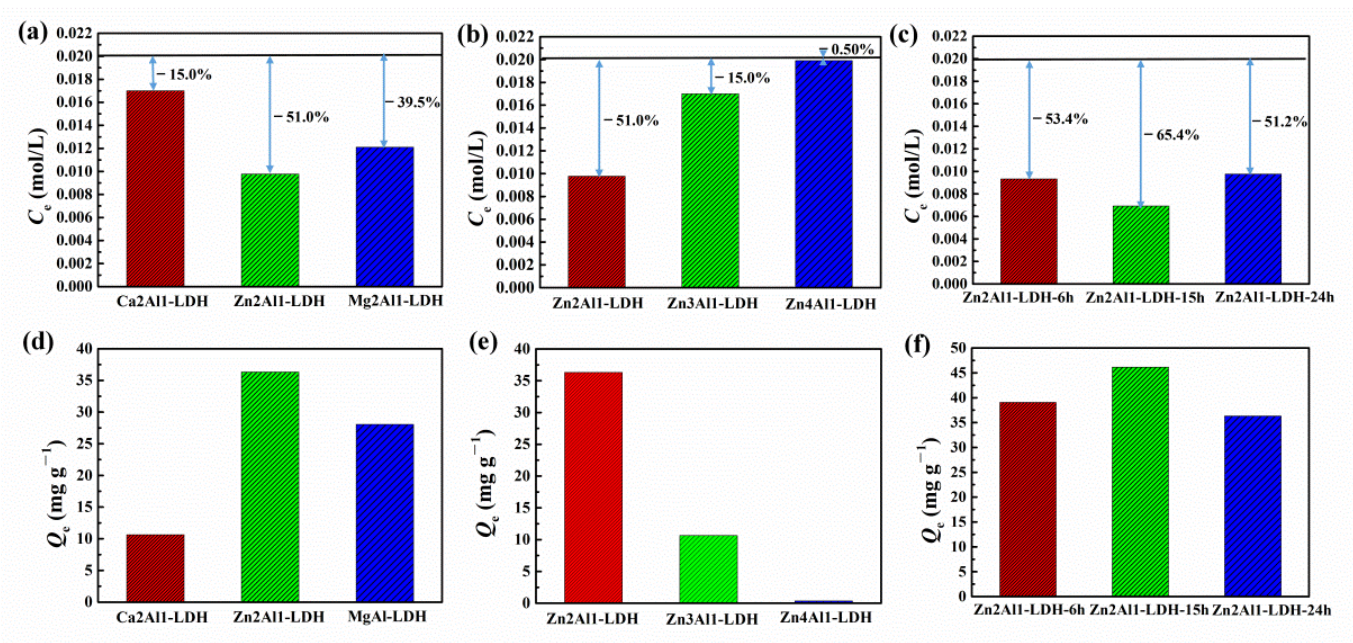

Figure 10. The equilibrium chloride concentration C_e (mol/L) (**a**) Ca2Al1-LDH, Zn2Al1-LDH and Mg2Al1-LDH; (**b**) Zn2Al1-LDH, Zn3Al1-LDH and Zn4Al1-LDH; (**c**) Zn2Al1-LDH-6 h, Zn2Al1-LDH-15 h and Zn2Al1-LDH-24 h and amount of chloride adsorption at the equilibrium Q_e (mg·g^{-1}) of different LDH samples in 0.02 mol/L NaCl; (**d**) Ca2Al1-LDH, Zn2Al1-LDH and Mg2Al1-LDH; (**e**) Zn2Al1-LDH, Zn3Al1-LDH and Zn4Al1-LDH; (**f**) Zn2Al1-LDH-6 h, Zn2Al1-LDH-15 h and Zn2Al1-LDH-24 h.

3.3. Morphology Characterization and Corrosion Protection Property of the Coatings

3.3.1. Coating Morphology and Roughness Characterization

The 3D morphology and roughness (arithmetical mean height) of different coating samples are listed in Figure 11. For the geometry of the samples being tested for roughness, the blank epoxy sample presented some large humps on the surface. The epoxy coating with addition of MgAl-LDH showed obvious pits, while the sample with ZnAl-LDH and CaAl-LDH demonstrated similar humps to that of the blank sample and minor defects on the sample surface. It can be seen from Figure 11a that the surface of the blank epoxy coatings was almost smooth, with the average roughness value of 0.318 ± 0.033 μm. It is worthy to note that there are many defects on the surface of the coating containing MgAl-LDH, as shown in Figure 11b. Correspondingly, its average roughness increased greatly to 1.031 ± 0.106 μm. This result indicated the bad compatibility of MgAl-LDH with the coating. As for the coating with ZnAl-LDH and CaAl-LDH, the surface seems similar to that of the blank epoxy coating and the roughness was measured to be 0.355 ± 0.055 μm and 0.330 ± 0.054 μm, respectively, which was close to the roughness value of the blank epoxy coating. The above result demonstrated that ZnAl-LDH and CaAl-LDH presented a better compatibility with the coating than MgAl-LDH.

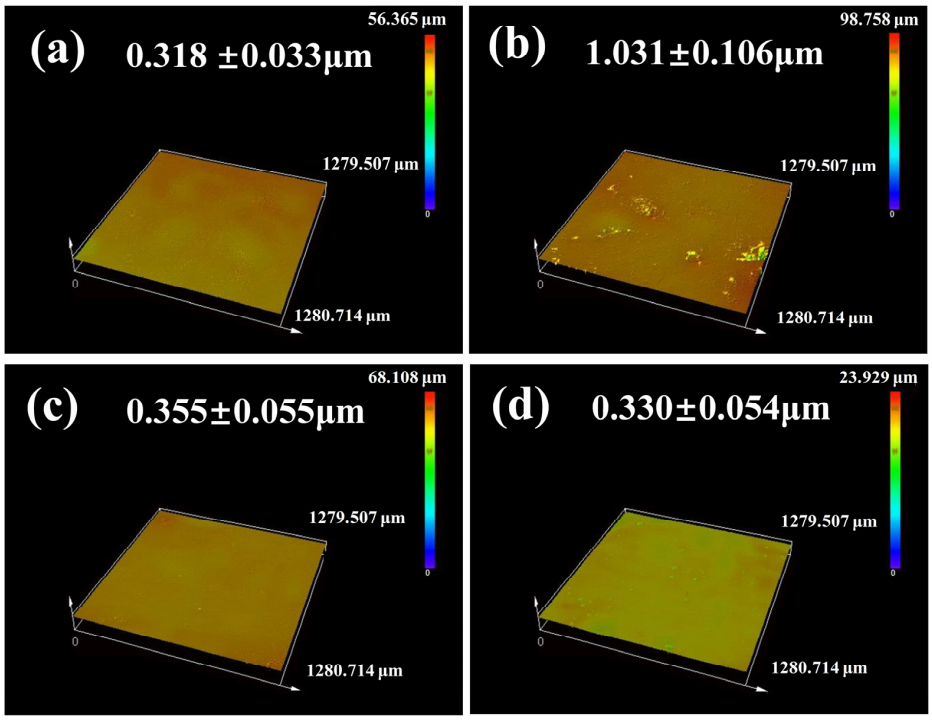

Figure 11. The 3D morphology and roughness (arithmetical mean height) of different coating samples (**a**) blank epoxy coating (**b**) epoxy coating with 2 wt.% MgAl-LDH (**c**) epoxy coating with 2 wt.% ZnAl-LDH (**d**) epoxy coating with 2 wt.% CaAl-LDH.

The top-view and side-view morphology of coatings with and without the addition of LDHs is shown in Figure 12. According to the top-view morphology, the blank epoxy coating showed some micro-cracks or defects on its surface. The side-view morphology of the blank epoxy coating showed some holes, as indicated by the green arrows. For the sample of the coating with 2% MgAl-LDH, some obvious aggregates can be seen on its surface as shown by the top-view morphology, in addition, some large blisters can be seen around the aggregates as indicated by the red arrows. Aggregates and increased holes can also be observed in the side-view morphology, suggesting a low compatibility with the epoxy coating, which is in good agreement with the 3D morphology and roughness result in Figure 11. For the coating with 2% ZnAl-LDH, there are some smaller aggregates with

smaller blisters in comparison with that of the coating with 2% MgAl-LDHs. As shown by the side-view morphology, lots of micro-cracks appeared. The top-view morphology of the epoxy coating with 2% CaAl-LDH showed small aggregates and almost no blisters can be seen, and its side-view image presented dense morphology without any cracks or holes, demonstrating a good compatibility of CaAl-LDH with the epoxy coating. It can be seen that the addition of CaAl-LDH was able to decrease defects in the coating and improved its compactness remarkably.

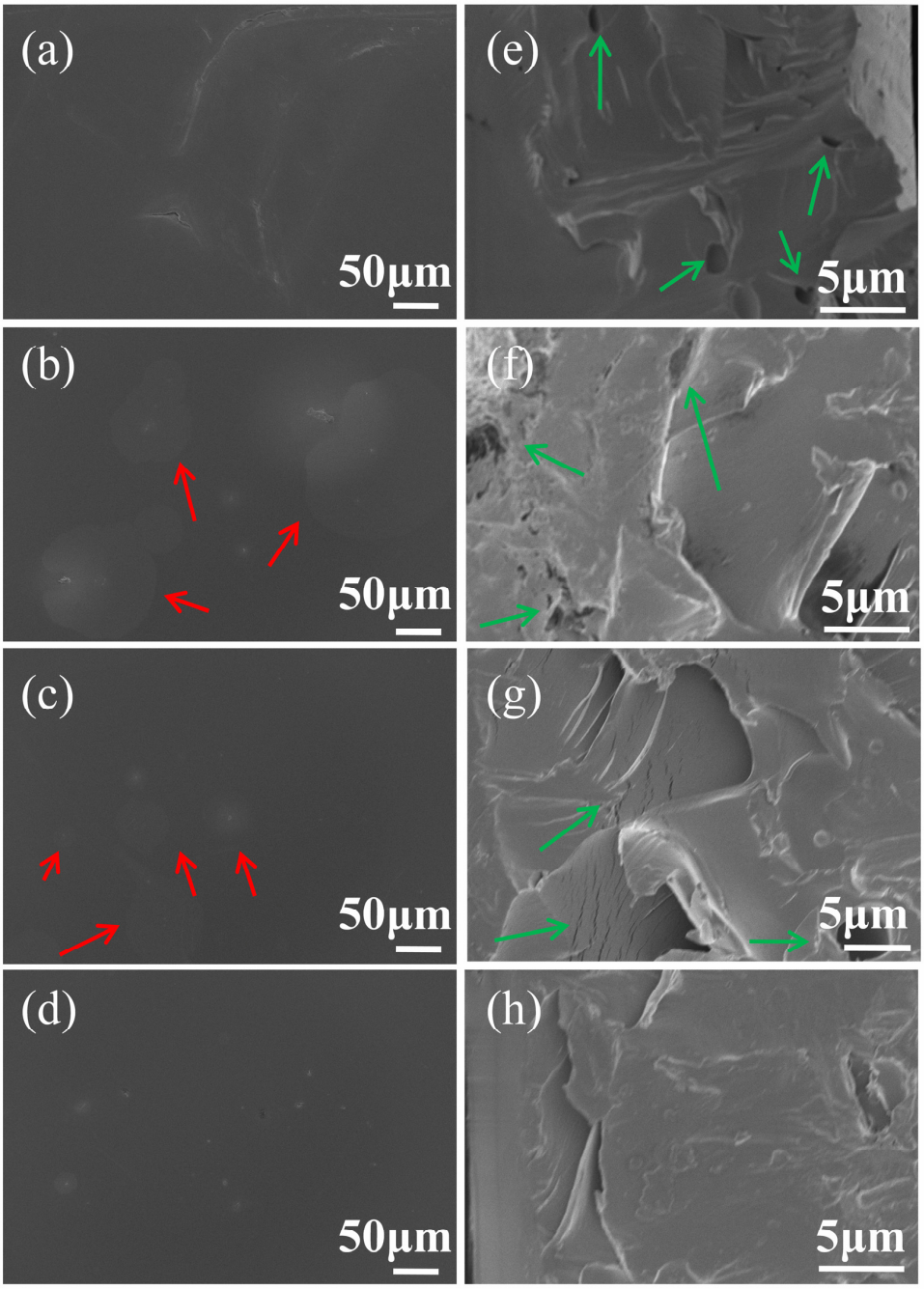

Figure 12. The top-view of coatings (**a**) without the addition of LDHs, (**b**) with addition of 2% MgAl-LDH, (**c**) with addition of 2% ZnAl-LDH and (**d**) addition of 2% CaAl-LDH; The side-view morphology of coatings (**e**) without the addition of LDHs, (**f**) with addition of 2% MgAl-LDH, (**g**) with addition of 2% ZnAl-LDH and (**h**) addition of 2% CaAl-LDH. (Please note that the blisters around the aggregates in the top-view morphologies were indicated by the red arrows and the holes and cracks in the side-view morphologies were indicated by the green arrows).

3.3.2. EIS Results

In order to investigate the corrosion protection ability of the synthesized samples and also the relationship between the chloride adsorption ability and the corrosion protection ability, Ca2Al1-LDH, Zn2Al1-LDH and Mg2Al1-LDH were incorporated into the epoxy coating with a weight percentage of 2.0% (vs. epoxy resin). The EIS measurements were carried out continually in a long immersion period of 21 days. The Nyquist and Bode plots were listed in Figures 13–16.

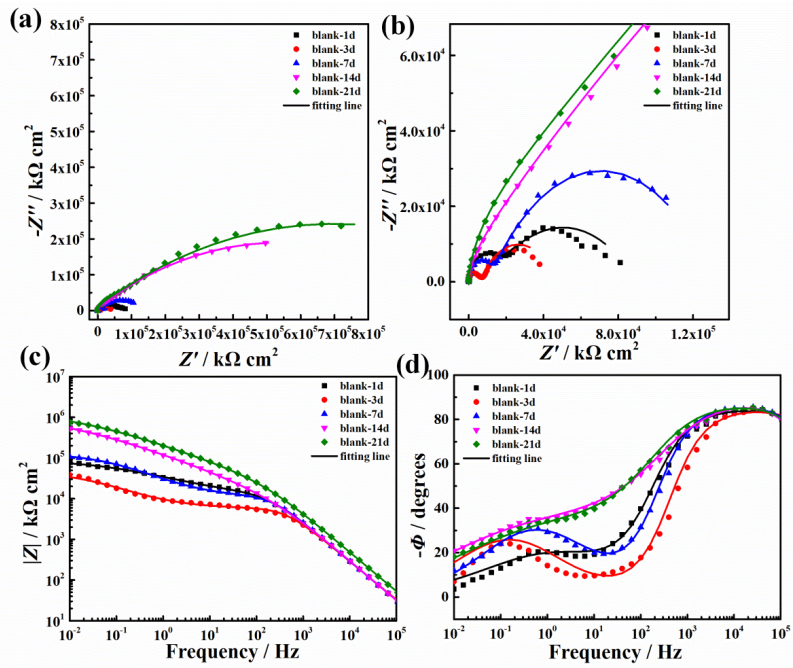

Figure 13. The Nyquist and Bode plots of the blank epoxy coating without addition of any LDHs samples during an immersion of 21 d (**a**) Nyquist plots; (**b**) magnification of Nyquist plots at high frequencies; (**c**) Impedance-frequency Bode plots; (**d**) Phase-frequency Bode plots.

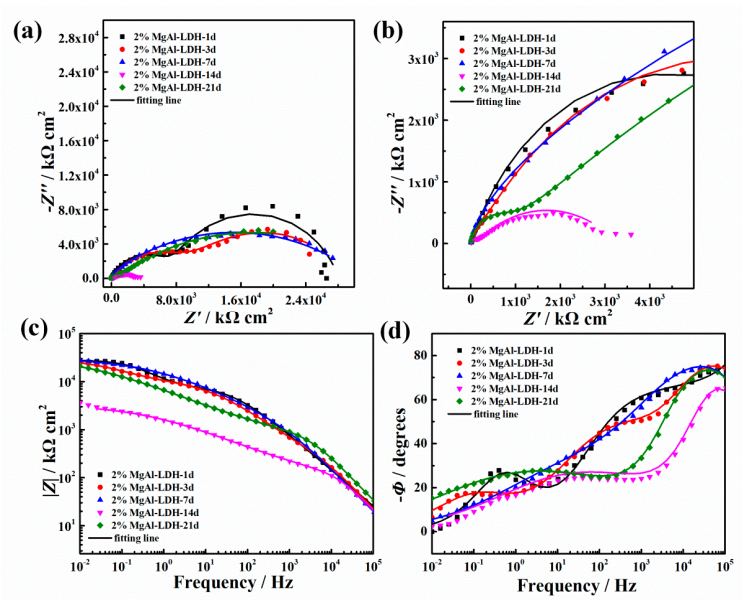

Figure 14. The Nyquist and Bode plots of the epoxy coating with addition of 2% MgAl-LDH during an immersion of 21 d (**a**) Nyquist plots; (**b**) magnification of Nyquist plots at high frequencies; (**c**) Impedance-frequency Bode plots; (**d**) Phase-frequency Bode plots.

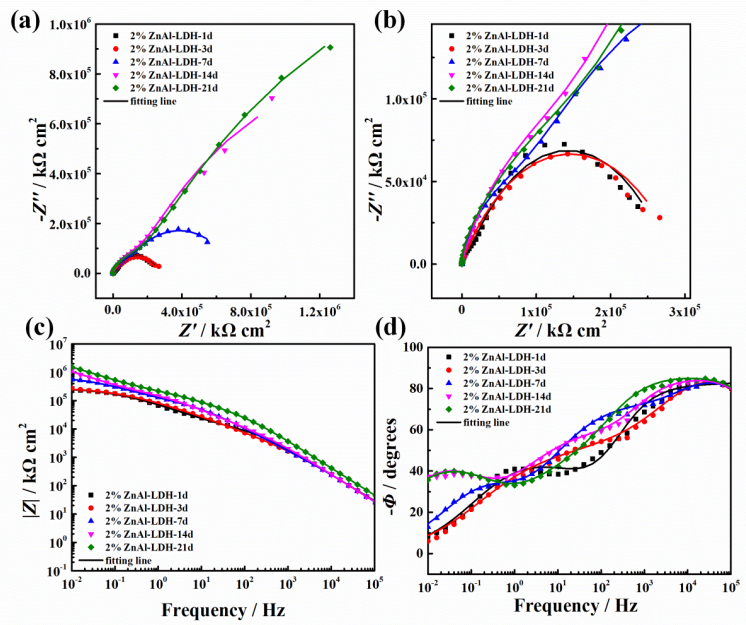

Figure 15. The Nyquist and Bode plots of the epoxy coating with addition of 2% ZnAl-LDH during an immersion of 21 d (**a**) Nyquist plots; (**b**) magnification of Nyquist plots at high frequencies; (**c**) Impedance-frequency Bode plots; (**d**) Phase-frequency Bode plots.

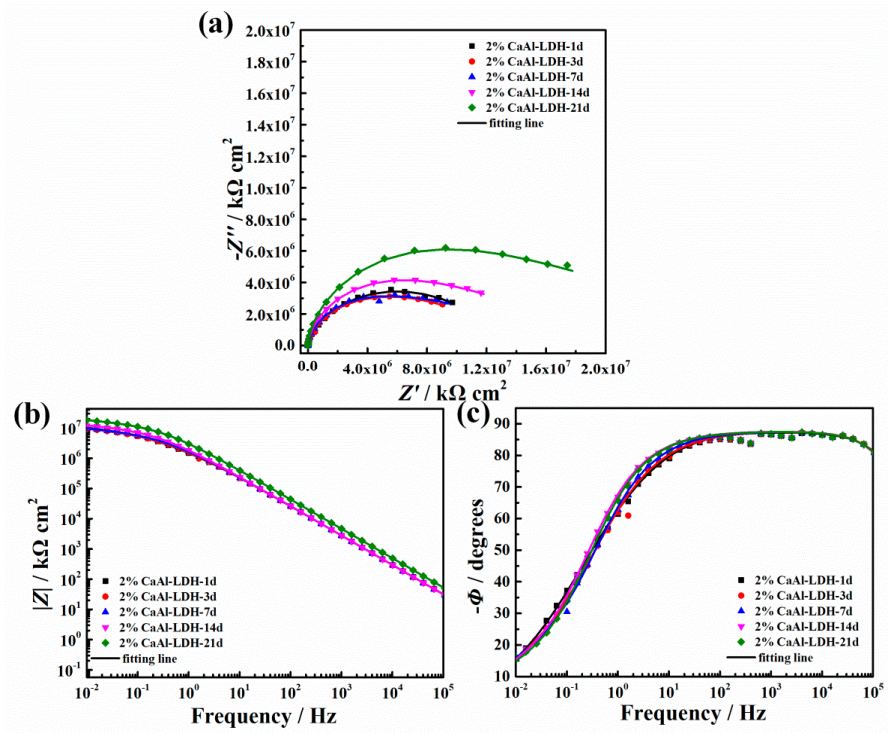

Figure 16. The Nyquist and Bode plots of the epoxy coating with addition of 2% CaAl-LDH during an immersion of 21 d (**a**) Nyquist plots; (**b**) Impedance-frequency Bode plots; (**c**) Phase-frequency Bode plots.

For the blank epoxy coating in Figure 13a,b, it can be seen that the impedance arc was small and increased gradually upon the immersion time. The impedance arcs of the sample at 14 d and 21 d were remarkably larger than that of the sample at 1–7 d, which can be attributed to the accumulation of the corrosion products, preventing the further propagation of the corrosion. In addition, there are two impedance arcs in the case of the sample at

1 d, 3 d and 7 d, one corresponding to the coating, and the other one corresponding to the charge transfer reaction in the metal/coating interface. This result indicated that corrosion occurred quickly after immersion for only 1 d, suggesting bad corrosion protection effect of the blank epoxy coating. After immersion for 14 d and 21 d, the two arcs were not obvious, which was caused by the accumulation of the corrosion products. According to Figure 12c, the impedance of the sample at 1–7 d at low frequency (0.01 Hz) was around 1×10^5 kΩ·cm^2, while this value increased to more than 5×10^5 kΩ cm^2 after immersion for 14 d and 21 d. It can be seen from Figure 12d that two phase angle peaks appeared in the Bode plots, therefore, an equivalent circuit including two-time constants in Figure 17a was used to fit the EIS data of this sample, where R_s is the solution resistance, R_c and R_{ct} present the coating resistance and the charge transfer resistance, respectively. CPE_c and CPE_{dl} stand for the constant phase elements of the coating and the double layer [8,43].

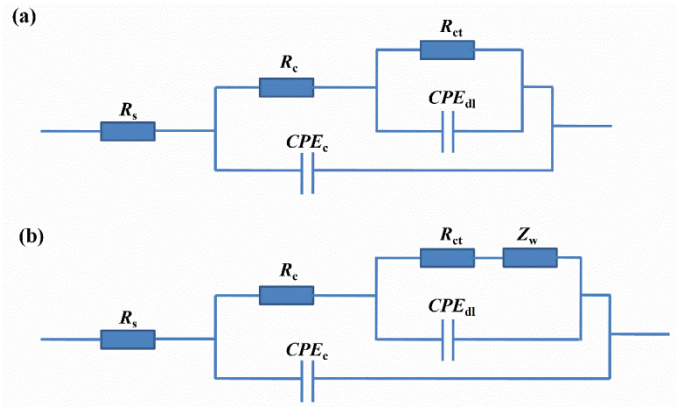

Figure 17. Equivalent circuits used to fit the EIS data in Figures 13–16. (**a**) with two time constants; (**b**) with three time constants.

The EIS results of the epoxy coating with the addition of 2% MgAl-LDH are listed in Figure 14. According to Figure 14a, this sample presented two impedance arcs and the impedance arcs kept almost constant upon the increased immersion time. The impedance at low frequencies (0.01 Hz) in Figure 14c was around 2.5×10^4 kΩ cm^2, which was lower than that of the blank epoxy sample. This result indicated that the addition of MgAl-LDH may produce some destructive effect for the coating quality rather than improve the corrosion protection effect. It can be seen that there are three phase angle peaks in Figure 14d, therefore, the equivalent circuit containing three-time constants in Figure 17b was used to fit the corresponding EIS data. The additional time constant can be attributed to the Warburg-diffusion impedance, and its appearance indicated the serious corrosion in this system [44].

The EIS spectra of the epoxy sample with 2% ZnAl-LDH was listed in Figure 15. According to Figure 15a, the impedance arc increased gradually upon the increased immersion time, which can be attributed to the physical barrier effect of the accumulated corrosion product and the inhibiting effect of the released Zn^{2+} cations. It is clear from Figure 15c that the impedance at low frequencies increased from 2.0×10^5 kΩ cm^2 to 1.6×10^6 kΩ cm^2 when the immersion time was increased from 1 d to 21 d, which was higher than that of the blank epoxy coating. This result indicated an enhanced corrosion protection effect of ZnAl-LDH in the epoxy coating. The Bode plots in Figure 15d also showed three phase angle peaks, therefore, the equivalent circuit with three-time constants in Figure 17b was used to fit the EIS data with the additional time constant corresponding to the Warburg-diffusion impedance.

Figure 16 shows the EIS results of the epoxy coating with addition of 2% CaAl-LDH during an immersion of 21 d. It can be seen from Figure 16a,b that the impedance arc and the impedance values at low frequencies remained almost constant during an immersion period of 1 d to 7 d. With time going on, the impedance arc became larger and the impedance

value at low frequencies reached 1.8 × 10^7 kΩ cm^2 after immersion for 21 d, which is more than one magnitude higher than that of the blank epoxy coating, demonstrating superior corrosion protection ability of CaAl-LDH. Although it seems that there was only one phase angle peak in Figure 16c, the presence of this broad peak was possibly due to the overlapping of two separate phase angle peaks, where one corresponded to the epoxy coatings and the other was related to the corrosion process. Similar to the blank epoxy coating, the equivalent circuit with two-time constants in Figure 17a was adopted to fit the EIS data, where one time constant was related to the coating, and the other corresponded to the charge transfer process in the coating/substrate interface, respectively.

Two parameters of low-frequency impedance modulus ($|Z|_{10mHz}$) and breakdown frequency (frequency changes at the phase angle of −45° (f_b)) were directly derived from the EIS diagrams, and the corresponding results are shown in Figure 18a,b, respectively. According to Figure 18a, the $|Z|_{10mHz}$ value of the sample with 2% MgAl-LDH showed a decreasing changing trend with the increase of the immersion time while the other three samples presented a rising variation trend. The $|Z|_{10mHz}$ value of the sample with 2% CaAl-LDH reached a level of 10^7 kΩ cm^2 during the immersion period, which is more than one magnitude higher than that of the blank epoxy coating sample and the sample with 2% ZnAl-LDHs, indicating the significantly enhanced corrosion protection effect of CaAl-LDHs in coatings. Based on the literature, f_b can be changed when organic coating delamination occurs caused by the permeation of aggressive medium [45]. It can be seen that the f_b values of the sample with 2% MgAl-LDH increased upon the immersion time, which may be related to the continuous penetration of corrosive species. It is worthy to note that the f_b values of the sample with 2% CaAl-LDH almost remained unchanged during the immersion time. The presence of CaAl-LDH may improve the barrier effect of the coating and reduce the corrosion product volume, therefore, the epoxy coating delamination was prevented significantly. As for the variation trend of R_c and R_{ct} in Figure 18c,d, the sample with 2% CaAl-LDH showed the highest R_c and R_{ct} values in comparison with other samples. The values of these two parameters were similar in the case of the blank epoxy coating and the coating with 2% ZnAl-LDH. The sample with 2% MgAl-LDH presented a lowest R_c and R_{ct} values, indicating an accelerating corrosion effect rather than improved corrosion protection due to a bad compatibility with the coating as shown by Figures 11 and 12.

The impedance of a *CPE* is defined by Equation (2) [8]:

$$Z_{CPE} = [Y_0(jw)^n]^{-1} \quad (2)$$

where Y_0 is the modulus, w is the angular frequency, and n refers to the dimensionless index, C_c and C_{dl} can be calculated from Equation (3) [8,35]:

$$C = [Y_0{}^* \cdot R^{1-n}]^{1/n} \quad (3)$$

C_c is an indicator of water uptake in the coatings and C_{dl} measures the numbers of the electrochemically active sites in the coating/substrate interface [44]. According to the C_c and C_{dl} results in Figure 18c,d, the C_c and C_{dl} of the sample with 2% CaAl-LDH presented relatively low values during the immersion period, indicating that the corrosion of metal substrate was prevented much more effectively, in comparison with other samples. It can be seen that the result in Figure 18a–f was consistent with each other, and it can be concluded that the 2% CaAl-LDH is able to provide significantly enhanced corrosion protection effect for the epoxy coatings.

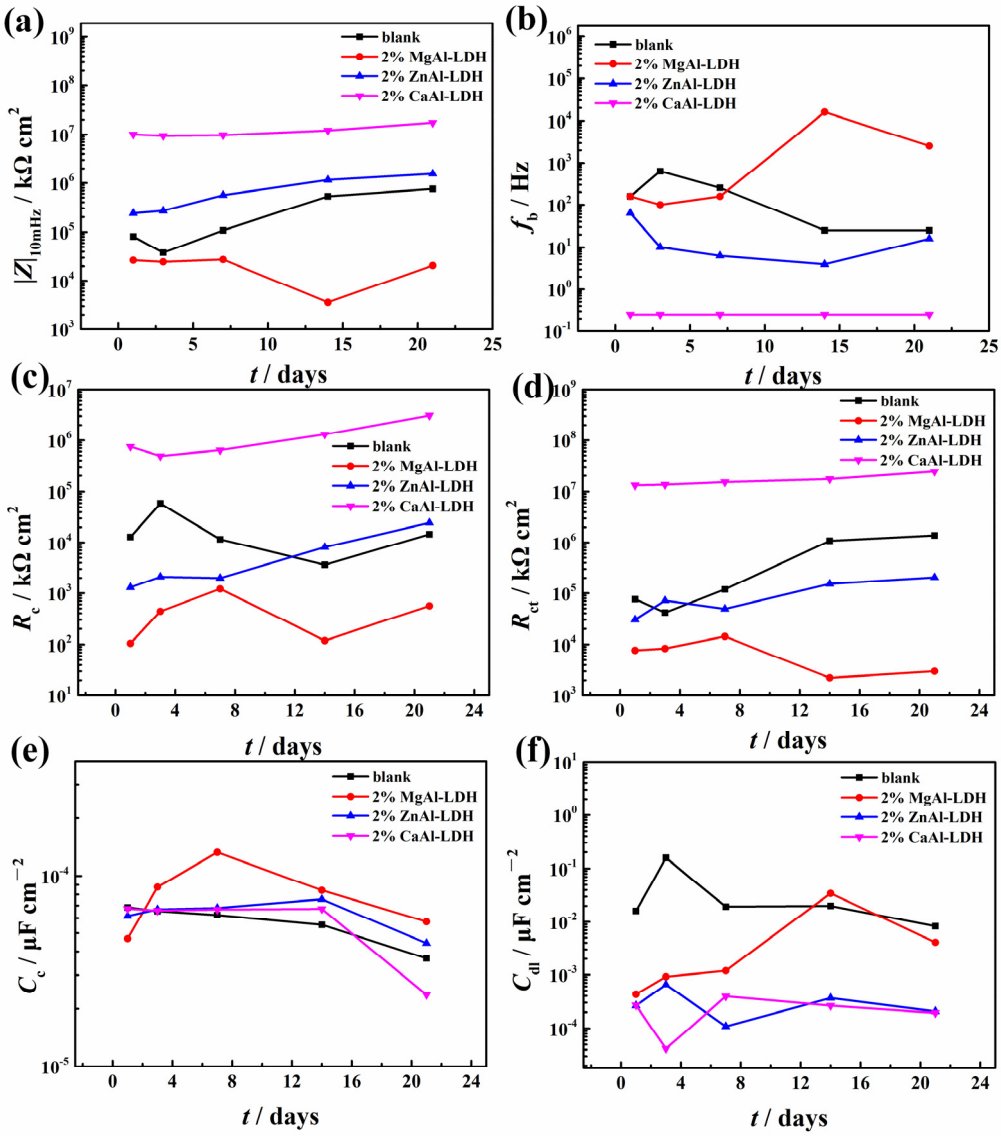

Figure 18. The variation of different EIS parameters (**a**) The impedance at 10 mHz; (**b**) breakdown frequency (frequency changes at the phase angle of −45°(f_b)); (**c**) coating resistance (R_c); (**d**) charge transfer resistance (R_{ct}); (**e**) coating capacitance (C_c); (**f**) double layer capacitance (C_{dl}) with the increase of the immersion time.

3.3.3. Salt Spray Test Results

Different epoxy coating samples were subjected to the neutral salt spray test to further evaluate their corrosion protection abilities. Optical images were captured at fixed time to record the surface changes of the coatings. The results are shown in Figure 19 and the corrosion spots were indicated by the red circles. It can be seen that no corrosion spots can be seen on all the samples after the salt spray test duration of 3 d. After 7 d, slight corrosion can be observed on the coating with 2% MgAl-LDH and corrosion became serious after 14 d. Corrosion can also be seen clearly on the surface of the blank epoxy coatings and the coating with 2% ZnAl-LDHs after 14 d. After salt spray test of 21 d, corrosion further propagated on the blank epoxy coatings, the coatings with 2% MgAl-LDH and 2% ZnAl-LDH, while only a few small corrosion spots can be observed on the surface of the coatings with 2% CaAl-LDH. The result indicated that the addition of MgAl-LDH accelerated corrosion and ZnAl-LDH provided negligible corrosion protection in the coatings probably due to the bad compatibility, while CaAl-LDH provided significant corrosion protection enhancement for the coatings. This result was in good accordance with the EIS results.

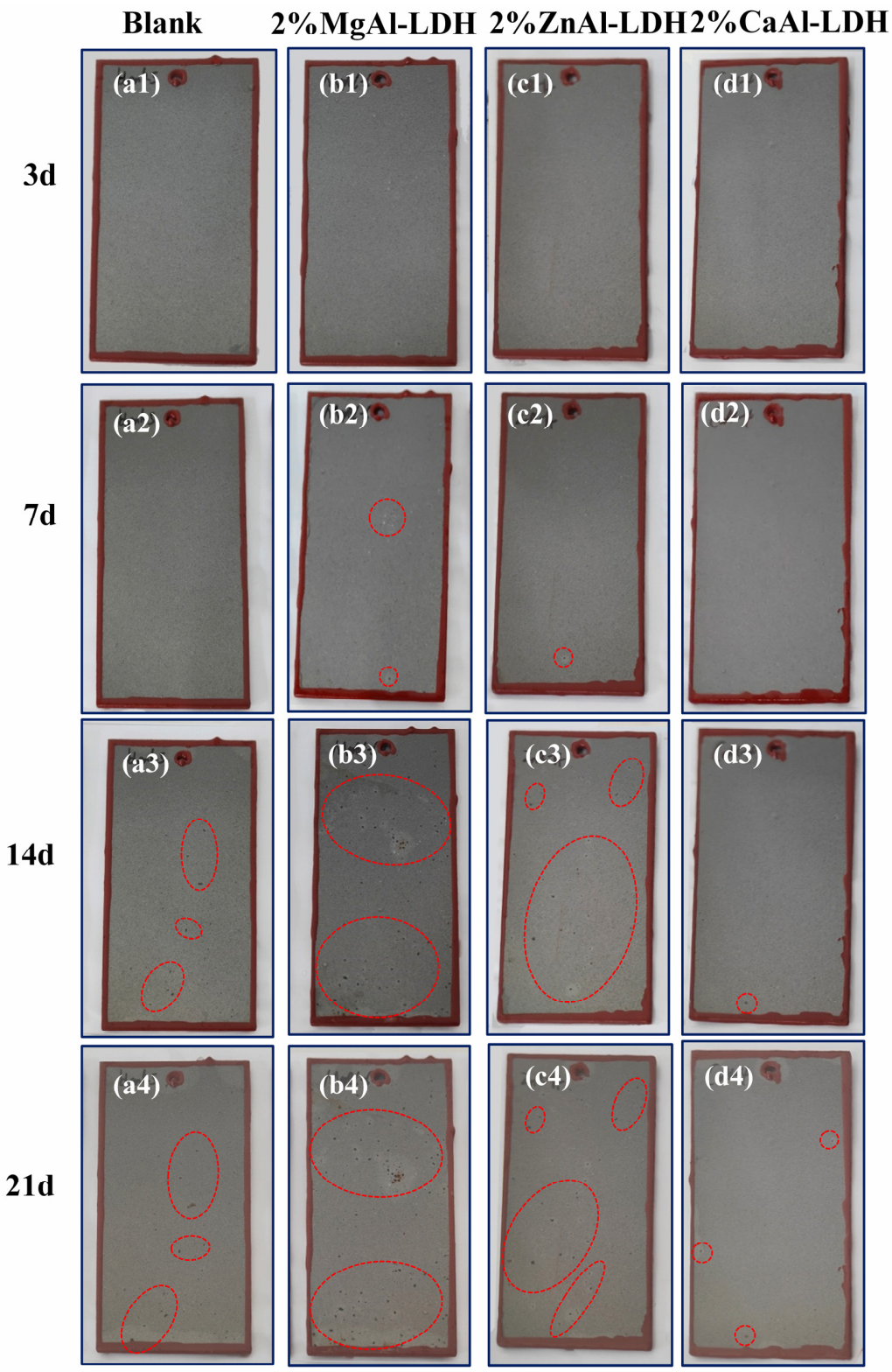

Figure 19. The optical images of different coating samples after exposure for various time (**a1**–**a4**). The sample with blank epoxy coatings at 3 d, 7 d, 14 d and 21 d; (**b1**–**b4**) The sample with epoxy coatings containing 2% MgAl-LDH at 3 d, 7 d, 14 d and 21 d; (**c1**–**c4**) The sample with epoxy coatings containing 2% ZnAl-LDH at 3 d, 7 d, 14 d and 21 d; (**d1**–**d4**) The sample with epoxy coatings containing 2% CaAl-LDH at 3 d, 7 d, 14 d and 21 d.

3.4. Corrosion Protection Mechanism

Based on the above discussion, the possible working mechanism of different LDHs sample in coatings is presented in Figure 20. As can be seen from Figure 20a, some cracks and holes appeared in the blank epoxy coating, which provided sites for the permeation of water molecules and chloride anions in the aggressive medium. After the aggressive medium reached the interface between the coating and the metal substrates, corrosion was initiated, and corrosion products were formed. In the case of the coating with the addition of MgAl-LDH (Figure 20b), serious aggregation of MgAl-LDH occurred and lots of holes were induced in this system due to the corporation of MgAl-LDH. Although some chlorides were adsorbed due to the anion-exchange reaction between the chlorides in the environment and the interlayer nitrates in the LDH interlayer space, the positive effect was negligible in comparison with the negative effect caused by the poor compatibility of the MgAl-LDH in the coatings. In Figure 20c, lots of new micro-cracks appeared due to the incorporation of ZnAl-LDH based on the SEM result in Figure 12, and corrosion was as serious as that in the case of the blank epoxy coating caused by the bad compatibility in spite of the highest chloride adsorption ability among all the LDHs samples. As for the coating with CaAl-LDH (Figure 20d), CaAl-LDH platelets were dispersed well in the epoxy coating and some holes and/or cracks can be filled, and the diffusion paths of the water molecules and chlorides can be extended in this way, and it will be more difficult for them to reach the coating/metal interface. As a result, corrosion will be harder to be initiated. It can be seen that CaAl-LDH platelets demonstrated effective corrosion protection effect in the epoxy coating for the underlying substrates despite that they showed lower chloride adsorption ability than other LDHs samples. This finding indicated that the barrier effect of LDHs in the coatings played a much more significant role in the overall corrosion protection effect in comparison with the chloride trapping effect.

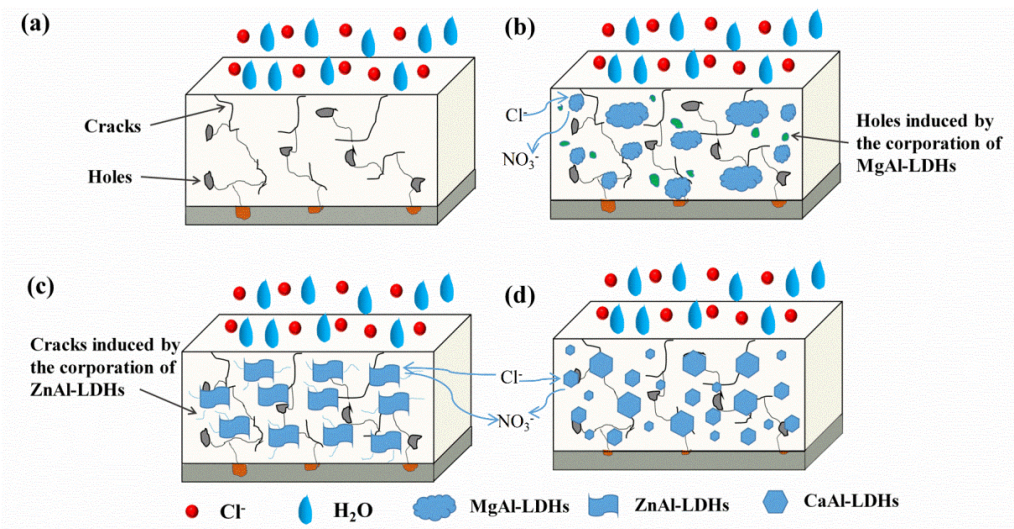

Figure 20. The schematic illustration of the corrosion protection mechanism (**a**) blank epoxy coating; (**b**) epoxy coating with 2% MgAl-LDH; (**c**) epoxy coating with 2% ZnAl-LDH; (**d**) epoxy coating with 2% CaAl-LDH.

4. Conclusions

Several points of conclusions can be drawn as follows:

(1) The influence of important synthesizing parameters including different divalent cations, divalent to trivalent cation ratios and hydrothermal time on the morphology, composition and structure was investigated. It was found that the increase of divalent to trivalent cation ratios and hydrothermal time led to the formation of more ZnO, resulting in the lower chloride adsorption ability.

(2) The relationship between the chloride adsorption ability of LDHs synthesized with different parameters and the finally obtained corrosion protection property of the epoxy coatings was deeply explored. Although ZnAl-LDH presented higher chloride adsorption ability, the epoxy coating with the addition of CaAl-LDH showed a better corrosion protection effect. The result indicated that the observed corrosion property was not directly proportional to the measured chloride adsorption ability.

(3) It can be concluded that the corrosion protection property was influenced more significantly by the dispersion state and physical barrier effect of the additions, which emphasizes the physical barrier role of LDHs rather than the chloride adsorption ability in coatings. However, the result may become different when corrosion inhibitors were intercalated in the LDH gallery, and we will focus on this point in the future work.

Author Contributions: Conceptualization, Y.C. and K.C.; Investigation, Y.C. and S.F.; Writing—original draft preparation, Y.C. Funding acquisition, Y.C. and Y.L. Writing—review & editing, J.W.; Supervision, J.W.; Resources, K.C.; Formal analysis, X.Z.; Methodology, X.Z.; Software, B.Z. and X.W.; Data curation, S.F. and Y.L.; Project administration, C.H. All authors have read and agreed to the published version of the manuscript.

Funding: This research was funded by State Key Laboratory for Marine Corrosion and Protection Foundation (JS220902) and Xiamen Science and Technology Plan Project (3502ZCQ20201002).

Institutional Review Board Statement: Not applicable.

Informed Consent Statement: Not applicable.

Data Availability Statement: The raw/processed data required to reproduce these findings will be shared by the corresponding author upon reasonable request.

Conflicts of Interest: The authors declare no conflict of interest.

References

1. Yohai, L.; Vázquez, M.; Valcarce, M. Phosphate ions as corrosion inhibitors for reinforcement steel in chloride-rich environments. *Electrochim. Acta* **2013**, *102*, 88–96. [CrossRef]
2. Serdechnova, M.; Mohedano, M.; Kuznetsov, B.; Mendis, C.L.; Starykevich, M.; Karpushenkov, S.; Tedim, J.; Ferreira, M.; Blawert, C.; Zheludkevich, M. PEO coatings with active protection based on in-situ formed LDH-nanocontainer. *J. Electrochem. Soc.* **2016**, *164*, C36–C45. [CrossRef]
3. Chen, C.; Qiu, S.; Cui, M.; Qin, S.; Yan, G.; Zhao, H.; Wang, L.; Xue, Q. Achieving high performance corrosion and wear resistant epoxy coatings via incorporation of noncovalent functionalized graphene. *Carbon* **2017**, *114*, 356–366. [CrossRef]
4. Yabuki, A.; Okumura, K. Self-healing coatings using superabsorbent polymers for corrosion inhibition in carbon steel. *Corros. Sci.* **2012**, *59*, 258–262. [CrossRef]
5. Liu, J.; Zhang, Y.; Yu, M.; Li, S.; Xue, B.; Yin, X. Influence of embedded ZnAlCe-NO_3^- layered double hydroxides on the anticorrosion properties of sol–gel coatings for aluminum alloy. *Prog. Org. Coat.* **2015**, *81*, 93–100. [CrossRef]
6. Rodriguez, J.; Bollen, E.; Nguyen, T.D.; Portier, A.; Paint, Y.; Olivier, M.G. Incorporation of layered double hydroxides modified with benzotriazole into an epoxy resin for the corrosion protection of Zn-Mg coated steel. *Prog. Org. Coat.* **2020**, *149*, 105894. [CrossRef]
7. Mei, Y.; Xu, J.; Jiang, L.; Tan, Q. Enhancing corrosion resistance of epoxy coating on steel reinforcement by aminobenzoate intercalated layered double hydroxides. *Prog. Org. Coat.* **2019**, *134*, 288–296. [CrossRef]
8. Tabish, M.; Zhao, J.; Wang, J.; Anjum, M.J.; Qiang, Y.; Yang, Q.; Mushtaq, M.A.; Yasin, G. Improving the corrosion protection ability of epoxy coating using CaAl LDH intercalated with 2-mercaptobenzothiazole as a pigment on steel substrate. *Prog. Org. Coat.* **2022**, *165*, 106765. [CrossRef]
9. Zaghloul, M.; Mohamed, Y.; El-Gamal, H. Fatigue and tensile behaviors of fiber-reinforced thermosetting composites embedded with nanoparticles. *J. Compos. Mater.* **2018**, *53*, 709–718. [CrossRef]
10. Zaghloul, M. Mechanical properties of linear low-density polyethylene fire-retarded with melamine polyphosphate. *J. Appl. Polym. Sci.* **2018**, *135*, 46770. [CrossRef]
11. Xue, B.; Yu, M.; Liu, J.; Li, S.; Xiong, L.; Kong, X. Synthesis of inhibitor nanocontainers with two-dimensional structure and their anticorrosion action in sol-gel coating on AA2024-T3 aluminum alloy. *J. Electrochem. Soc.* **2017**, *164*, C641–C652. [CrossRef]
12. Nguyen, T.D.; Nguyen, A.S.; Tran, B.A.; Vu, K.O.; Tran, D.L.; Phan, T.T.; Scharnagl, N.; Zheludkevich, M.L. To TXH Molybdate intercalated hydrotalcite/graphene oxide composite as corrosion inhibitor for carbon steel. *Surf. Coat. Technol.* **2020**, *399*, 126165. [CrossRef]

13. Zhang, M.; Xu, F.; Lin, D.; Peng, J.; Zhu, Y. Wang H A smart anti-corrosion coating based on triple functional fillers. *Chem. Eng. J.* **2022**, *446*, 137078. [CrossRef]
14. Cao, Y.; Dong, S.; Zheng, D.; Wang, J.; Zhang, X.; Du, R.; Song, G.; Lin, C. Multifunctional inhibition based on layered double hydroxides to comprehensively control corrosion of carbon steel in concrete. *Corros. Sci.* **2017**, *126*, 166–179. [CrossRef]
15. Cao, Y.; Zheng, D.; Dong, S.; Zhang, F.; Lin, J.; Wang, C.; Lin, C. A composite corrosion inhibitor of MgAl layered double hydroxides co-intercalated with hydroxide and organic anions for carbon steel in simulated carbonated concrete pore solutions. *J. Electrochem. Soc.* **2019**, *166*, C3106–C3113. [CrossRef]
16. Cao, Y.; Zheng, D.; Luo, J.; Zhang, F.; Dong, S.; Pan, J.; Lin, C. Insight into the Fabrication of ZnAl Layered Double Hydroxides Intercalated with Organic Anions and Their Corrosion Protection of Steel Reinforced Concrete. *J. Electrochem. Soc.* **2019**, *166*, C617–C623. [CrossRef]
17. Cao, Y.; Zheng, D.; Li, X.; Lin, J.; Wang, C.; Dong, S.; Lin, C. Enhanced corrosion resistance of superhydrophobic layered double hydroxide films with long-term stability on Al substrate. *ACS Appl. Mater. Interfaces* **2018**, *10*, 15150–15162. [CrossRef]
18. Cao, Y.; Zheng, D.; Luo, J.; Zhang, F.; Wang, C.; Dong, S.; Ma, Y.; Liang, Z.; Lin, C. Enhanced corrosion protection by Al surface immobilization of in-situ grown layered double hydroxide films co-intercalated with inhibitors and low surface energy species. *Corros. Sci.* **2020**, *164*, 108340. [CrossRef]
19. Cao, Y.; Zheng, D.; Lin, C. Construction of ecofriendly anticorrosive composite film ZnAl-LDH by modification of lignin onAA7075 surface. *Mater. Corros.* **2021**, *72*, 1595–1606. [CrossRef]
20. Iqbal, M.A.; Sun, L.; Asghar, H.; Fedel, M. Chlorides Entrapment Capability of Various In-Situ Grown NiAl-LDHs: Structural and Corrosion Resistance Properties. *Coatings* **2020**, *10*, 384. [CrossRef]
21. Wang, Y.; Huang, Q.; Zhou, B.; Yuan, Z.; Wei, Y.; Fujita, T. Corrosion Protection of 6061 Aluminum Alloys by Sol-Gel Coating Modified with ZnLaAl-LDHs. *Coatings* **2021**, *11*, 478. [CrossRef]
22. Cao, Y.; Fang, S.; Chen, K.; Qi, H.; Zhang, X.; Huang, C.; Wang, J.; Liu, J. Insight into the Preparation of MgAl-Layered Double Hydroxide (LDH) Intercalated with Nitrates and Chloride Adsorption Ability Study. *Appl. Sci.* **2022**, *12*, 4492. [CrossRef]
23. Chen, M.; Wu, F.; Yu, L.; Cai, Y.; Chen, H.; Zhang, M. Chloride binding capacity of LDHs with various divalent cations and divalent to trivalent cation ratios in different solutions. *CrystEngComm* **2019**, *21*, 6790–6800. [CrossRef]
24. Zhu, A.; Wang, H.; Xue, M.; Cao, Y.; He, J.; Lu, W.; Xu, Y.; Zeng, B.; Yuan, C.; Chen, G.; et al. Preparation of two-dimensional boron nitride-layered double hydroxide hybrid to reinforce the corrosion protection of the epoxy coating. *Mater. Corros.* **2022**, *73*, 1444–1458. [CrossRef]
25. *ISO 16773-2016*; Electrochemical Impedance Spectroscopy (EIS) on Coated and Uncoated Metallic Specimens. ISO: Geneva, Switzerland, 2016.
26. *GB/T 1771-2007*; Paints and Varnishes—Determination of Resistance to Neutral Salt Spray (Fog). China National Standardization Administration: Beijing, China, 2007.
27. Zheludkevich, M.L.; Poznyak, S.K.; Rodrigues, L.M.; Raps, D.; Hack, T.; Dick, L.F.; Nunes, T.; Ferreira, M. Active protection coatings with layered double hydroxide nanocontainers of corrosion inhibitor. *Corros. Sci.* **2010**, *52*, 602–611. [CrossRef]
28. Zhou, M.; Pang, X.; Wei, L.; Gao, K. Insitu grown superhydrophobic Zn–Al layered double hydroxides films on magnesium alloy to improve corrosion properties. *Appl. Surf. Sci.* **2015**, *337*, 172–177. [CrossRef]
29. Guo, X.; Xu, S.; Zhao, L.; Lu, W.; Zhang, F.; Evans, D.G.; Duan, X. One-step hydrothermal crystallization of a layered double hydroxide/alumina bilayer film on aluminum and its corrosion resistance properties. *Langmuir* **2009**, *25*, 9894–9897. [CrossRef]
30. Hu, T.; Ouyang, Y.; Xie, Z.; Wu, L. One-pot scalable in situ growth of highly corrosion-resistant MgAl-LDH/MBT composite coating on magnesium alloy under mild conditions. *J. Mater. Sci. Technol.* **2021**, *92*, 225–235. [CrossRef]
31. Zuo, J.D.; Peng, Z.C.; Dong, B.Q.; Wang, Y.S. In situ growth of corrosion resistant Mg-Fe layered double hydroxide film on Q235 steel. *J. Colloid Interf. Sci.* **2021**, *610*, 202–212. [CrossRef]
32. He, Q.Q.; Zhou, M.J.; Hu, J.M. Electrodeposited Zn-Al layered double hydroxide films for corrosion protection of aluminum alloys. *Electrochim. Acta* **2020**, *355*, 136796. [CrossRef]
33. Salak, A.N.; Tedim, J.; Kuznetsova, A.I.; Zheludkevich, M.L.; Ferreira, M. Anion exchange in Zn–Al layered double hydroxides: In situ X-ray diffraction study. *Chem. Phys. Lett.* **2010**, *495*, 73–76. [CrossRef]
34. Wu, Y.; Wu, L.; Zheludkevich, M.L.; Chen, Y.; Serdechnova, M.; Yao, W.; Blawert, C.; Atrens, A.; Pan, F. MgAl-$V_2O_7^{4-}$ LDHs/(PEI/MXene)10 composite film for magnesium alloy corrosion protection. *J. Mater. Sci. Technol.* **2021**, *91*, 28–39. [CrossRef]
35. Cao, Y.; Zheng, D.; Lin, C. Effect of physical barrier and anion-exchange process of nitrate-intercalated ZnAl layered double hydroxide films grown on Al on corrosion protection. *Surf. Coat. Technol.* **2021**, *421*, 127436. [CrossRef]
36. Tedim, J.; Kuznetsova, A.; Salak, A.N.; Montemor, F.; Snihirova, D.; Pilz, M.; Zheludkevich, M.L.; Ferreira, M. Zn–Al layered double hydroxides as chloride nanotraps in active protective coatings. *Corros. Sci.* **2012**, *55*, 1–4. [CrossRef]
37. Vieira, D.; Salak, A.; Ferreira, M.; Vieira, J.M.; Brett, C. Ce-substituted Mg-Al layered double hydroxides to prolong the corrosion protection lifetime of aluminium alloys. *Appl. Surf. Sci.* **2022**, *573*, 151527. [CrossRef]
38. Ren, L.; Gao, S.; Chen, Z.; Jiang, D.; Huang, H. Facile preparation of wear-resistant and anti-corrosion films on magnesium alloy. *Surf. Eng.* **2022**, *38*, 22–29. [CrossRef]
39. Li, Z.; Ba, Z.; Wang, T.; Kuang, J.; Jia, Y. Fabrication and characterization of Mg–Mn hydrotalcite films on pure Mg substrates. *Mater. Res. Express* **2019**, *6*, 116440. [CrossRef]

40. Zahedi, A.V.; Zhao, J.; Anjum, M.J.; Wei, S.; Wang, W.; Zhao, Z. The effect of cerium cation on the microstructure and anti-corrosion performance of LDH conversion coatings on AZ31 magnesium alloy. *J. Alloys Compd.* **2020**, *821*, 153248. [CrossRef]
41. Xu, J.; Song, Y.; Zhao, Y.; Jiang, L.; Mei, Y.; Chen, P. Chloride removal and corrosion inhibitions of nitrate, nitrite-intercalated Mg Al layered double hydroxides on steel in saturated calcium hydroxide solution. *Appl. Clay Sci.* **2018**, *163*, 129–136. [CrossRef]
42. Wei, J.; Xu, J.; Mei, Y.; Tan, Q. Chloride adsorption on aminobenzoate intercalated layered double hydroxides: Kinetic, thermodynamic and equilibrium studies. *Appl. Clay Sci.* **2020**, *187*, 105495. [CrossRef]
43. Tabish, M.; Zhao, J.; Kumar, A.; Yan, J.; Wang, J.; Shi, F.; Zhang, J.; Peng, L.; Mushtaq, M.A.; Yasin, G. Developing epoxy-based anti-corrosion functional nanocomposite coating with CaFe-Tolyl-triazole layered double hydroxide@g-C3N4 as nanofillers on Q235 steel substrate against NaCl corrosive environment. *Chem. Eng. J.* **2022**, *450*, 137624. [CrossRef]
44. Xu, T.; Zhao, Y.; Zhou, J.; Hu, J. Composite nanocontainers synthesized by in-situ growth of metal organic frameworks on layered double hydroxides having both passive and active protecting capabilities. *Prog. Org. Coat.* **2022**, *164*, 106695. [CrossRef]
45. Mohammadi, I.; Shahrabi, T.; Mahdavian, M.; Izadi, M. Construction of an epoxy coating with excellent protection performance on the AA 2024-T3 using ion-exchange materials loaded with eco-friendly corrosion inhibitors. *Prog. Org. Coat.* **2022**, *166*, 106786. [CrossRef]